

ABSTRACT

MEASUREMENT OF DIFFUSION CONSTANT AND TEMPERATURE IN COLD ATOMS VIA FLUORESCENCE IMAGING

by Daniel Christian Wingert

This thesis discusses the study of ultracold ^{85}Rb atoms in both molasses and optical lattices, with a focus on the implementation of a fluorescence imaging system to characterize diffusive motion of the atomic sample, and to measure temperature. Further, we show that our home-built camera and imaging system is capable of tracking sub-millisecond center-of-mass motion of the cold atom sample, by transiently applying a bias magnetic field that shifts the magneto-optical trap away from its equilibrium position. This is an important step toward our eventual goal of demonstrating a precisely controlled, directionally arbitrary ratchet in an optical lattice.

MEASUREMENT OF DIFFUSION CONSTANT AND TEMPERATURE IN COLD ATOMS
VIA FLUORESCENCE IMAGING

Thesis

Submitted to the
Faculty of Miami University
in partial fulfillment of
the requirements for the degree of
Master of Physics

by

Daniel Christian Wingert

Miami University

Oxford, Ohio

2023

Adviser: Samir Bali

Reader: Carlo Samson

Reader: Imran Mirza

©2023 Daniel Christian Wingert

This thesis titled

MEASUREMENT OF DIFFUSION CONSTANT AND TEMPERATURE IN COLD ATOMS
VIA FLUORESCENCE IMAGING

by

Daniel Christian Wingert

has been approved for publication by

College of Arts and Sciences

and

Department of Physics

Samir Bali

Carlo Samson

Imran Mirza

Contents

1	Introduction	1
1.1	Outline of Thesis	1
1.2	Motivation	2
1.3	Previous Work	3
2	Background	4
2.1	Optical Lattices	4
2.1.1	3D Tetrahedral Lattice	5
2.1.2	3D Inverted Umbrella Lattice	6
2.2	Data Collection Methods	8
2.2.1	Pump-Probe Spectroscopy	8
2.2.2	Fluorescence Imaging	10
3	Experimental Procedure	12
3.1	MOT and Molasses	12
3.1.1	Diffusion Constant and Temperature in Molasses	13
3.1.2	Perturbed MOT	17
3.2	3D Lattice	19
3.2.1	Pump-Probe Spectroscopy	19
3.2.2	Diffusion Constant and Temperature in 3D Lattice	20
3.3	Additional Experimental Techniques	22
3.3.1	Pixel to Centimeter Conversions	22

3.3.2	Fluorescence Imaging for MOT Atom Count	23
4	Results and Analysis	24
4.1	MOT and Molasses	24
4.1.1	Diffusion Constant and Temperature in Molasses	24
4.1.2	Perturbed MOT	29
4.2	3D Lattice	29
4.2.1	Pump-Probe Spectroscopy	30
4.2.2	Diffusion Constant and Temperature in 3D Lattice	34
5	Conclusion	38
5.1	Summary	38
5.2	Future Work	38
5.2.1	3D Ratchet in Inverted Umbrella Lattice	38
5.2.2	2D Directionally Arbitrary Ratchet	39
A	Suppressing Mode Hops in Commercial Laser Systems	41
B	MATLAB Analysis Codes	44
	Bibliography	56

List of Figures

2.1	Geometry of the 3D Tetrahedral Lattice, with the probe beam included in z as \vec{k}_p . The lattice beams are labelled as $\vec{k}_1 \rightarrow \vec{k}_4$, with polarization unit vectors labelled as e . $\theta_x = \theta_y \approx 25^\circ$	5
2.2	Geometry of the 3D Inverted Umbrella Lattice. The lattice beams are labelled $1 \rightarrow 4$, with the polarizations marked as $\epsilon_1 \rightarrow \epsilon_4$. In our experiment, $\theta = 25^\circ$. The right image is a projection onto the xy plane. Image taken from [8].	7
2.3	Data collected by the imaging system. On the left, we have the raw data taken by one experimental cycle. The middle shows background data collected by repeating this process, but with the imaging beam blocked. The right graph is created by subtracting the background from the raw data. The left and right graphs are scaled the same, while the y-axis on the background image is zoomed in to show detail. . .	11
3.1	Full timing diagram for a molasses diffusion imaging cycle. The top figure shows the LabVIEW display for 100ms molasses time and 30ms ballistic expansion time. The bottom figure shows the sequence in more detail. Δt_1 is the molasses time, and Δt_2 is the ballistic expansion time. Note the camera triggers on a falling edge. . . .	16
3.2	Full timing diagram for the perturbed MOT experiment. For this experiment, the B-grad line was rewired to the $-z$ Helmholtz coil. The top figure shows the LabVIEW display, and the bottom figure shows the sequence in more detail.	18
3.3	Geometry of probe beam for the umbrella lattice. The probe, in red, lies along the xz -plane. In our system, $\theta_p \approx 4.55^\circ$. Figure adapted from [8].	20

3.4	Full timing diagram for a lattice diffusion imaging cycle. The top figure shows the LabVIEW display, and the bottom figure shows the sequence in more detail.	21
3.5	Diagram demonstrating the setup used to determine pixel to centimeter conversion rates. The two lenses should have equal focal length. Note that the length f between the camera and the leftmost lens must extend to the photodiode of the camera, which is distinct from the front of the camera mount.	23
4.1	Plot of cloud area against molasses expansion time. The trap powers are set to a 40/40/20 relative intensity split, with the 20% corresponding to z	26
4.2	Relative locations for each value of β . For each value, the area is taken as the number of pixels above the line.	27
4.3	Plot of half the full width half max of the cloud against ballistic expansion time, after 10ms of molasses time. The trap powers are set to a 40/40/20 relative intensity split, with the 20% corresponding to z	28
4.4	Pump-probe spectrum taken in an inverted umbrella lattice at a detuning of 8.75 gamma and 16.25mW/cm ² axial intensity, 5.84mW/cm ² beam two and three intensity, and 5.42mW/cm ² beam four intensity, without any background subtraction. . .	30
4.5	Pump-probe spectrum taken in an inverted umbrella lattice at a detuning of 8.75 gamma and 16.25mW/cm ² axial intensity, 5.84mW/cm ² beam two and three intensity, and 5.42mW/cm ² beam four intensity, with the atomic cloud turned off by keeping the magnetic gradient off to capture background signal.	31
4.6	Pump-probe spectrum created by subtracting the background data from the raw data point by point. Peak Ω_z corresponds to the z -vibrational frequency, and peak Ω_x to the x -vibrational frequency.	32
4.7	Pump-probe spectrum taken in an inverted umbrella lattice at a detuning of 8.75 gamma and 16.25mW/cm ² axial intensity, 5.84mW/cm ² beam two and three intensity, and 5.42mW/cm ² beam four intensity, with a single lattice beam blocked. . . .	33
4.8	Graph of peak locations against $\sqrt{I/\Delta}$. The detuning is expressed as a dimensionless quantity scaled by the natural linewidth Γ , so the x -axis is given in units of $\sqrt{\text{mW/cm}^2}$. . .	33

4.9	Plot of cloud area against lattice expansion time. Data was taken in a 3D inverted umbrella lattice at a detuning of 8.75 gamma and 12.07mW/cm ² axial intensity, 4.34mW/cm ² beam two and three intensity, and 4.02mW/cm ² beam four intensity. .	34
4.10	Plot of half the full width half maximum against lattice expansion time. Data was taken in a 3D inverted umbrella lattice at a detuning of 8.75 gamma and 16.25mW/cm ² axial intensity, 5.84mW/cm ² beam two and three intensity, and 5.42mW/cm ² beam four intensity.	36
5.1	Geometry of the proposed 2D lattice. In the ideal case, $\theta = 120^\circ$, but the configuration of the vacuum chamber windows in our lab may result in a value of $\theta = 115^\circ$. Image taken from [9].	40
A.1	Image of the inside of the DLC. The dipswitches are in the bottom left, a bright red panel. The BIAS dipswitch is the fourth from the right.	43

To my Dad, whose constant belief has let me have the confidence to succeed.

and

To my Mom, whose constant love has helped me through every frustration.

Acknowledgements

No one achieves anything alone. This thesis took many more people than just me, and I'm gonna list as many as I can in a row on this page here. First, a *very* big thank you to Dr. Samir Bali for being a fantastic advisor and professor, from class my second day at Miami to the very last day here. Similarly, thank you to Alex Staron and Kefeng Jiang, the graduate students at the time I joined this lab, for imparting their wisdom and showing me great patience. Also, Krishna Pandey, my fellow survivor this year. Grant Brown is one of my best friends in the world and my best lab mate to date. Reese Tyra was as great as a roommate as he was in the lab. Casey Scoggins is acknowledged. The biggest thank you possible to Stone Oliver, without whom I would have had several (additional) mental breakdowns this summer. Chanakya Pandya and Luke Schmeltzer provided invaluable assistance this summer in collecting data and making vague references to TV shows Stone hadn't seen. Finally in terms of lab assistance, thank you so much to Mike Weeks and the rest of the Miami Instrumentation Lab for irreplaceable service provided. This work would not have been completed without your help. Outside of the lab, thank you so very much to both of my parents, for money, love, advice, and never-ending support as I worked through this degree. And last but most important, thank you to my fiancé Madeline Mae Booms for being the most amazing person who ever has or ever will exist, and bringing joy into my life no matter how hard work has been. Finally, thank you to every other friend, classmate, roommate, staff, and professor at Miami for providing me with an environment to learn and grow. The US Army Research Office is gratefully acknowledged for the funding it has provided.

Chapter 1

Introduction

The field of quantum optics and information has shown strong recent growth, with five Nobel prizes awarded in the field since 1997 alone. With the rapid discovery of new concepts and fundamental behaviors in the quantum realm, there have been a variety of different areas of research that one can pursue to advance the field. In particular, we are interested in the nanoscale transport of ultracold atoms as they interact with light. Our lab most recently performed an experimental demonstration of the concept of stochastic resonance in the directed propagation of ultracold rubidium atoms in an optical lattice [1]. Thus far, work has focused on a one-dimensional ratcheting motion along a single axis [2], and experimental work in our lab utilized the method of pump-probe spectroscopy to characterize atomic behavior. In the future, however, we hope to advance this work to the study of directionally arbitrary two-dimensional ratcheting, such as discussed in [3, 4]. In this thesis, I discuss the implementation of a fluorescence imaging system to observe 2D behavior, as well as several experiments that were performed using this technique.

1.1 Outline of Thesis

This thesis begins with a brief discussion of the motivation for this work, as well as related previous work both from this group as well as others. In chapter 2, I will discuss background information that provides context for the experiment, and in chapter 3 we discuss the specific experimental

designs and methods that were used for this thesis. In chapter 4, I mirror the layout of chapter 3, but discussing and analyzing the results that were collected from each experiment. Finally, in chapter 5, I summarize our findings, and discuss the planned future work that will build upon this thesis.

1.2 Motivation

As mentioned previously, this lab has historically utilized pump-probe spectroscopy to characterize the motion of cold atoms within an optical lattice. However, as I discuss in more detail in 2.2.1, this method of data collection is insufficient to observe the 2D motion that is the focus of future work. Atomic imaging, however, is a commonly used and theoretically simple data collection method that would be ideal for this work. In our lab, this method has been attempted before [5, 6], but it was found that the home-built laser systems at the time were not stable enough to produce accurate data. With the recent implementation of a commercial laser system, however, the stability of the cloud has improved, resulting in data sets that are reproducible and significantly less noisy. Therefore, in this thesis we first perform experiments in order to confirm the accuracy of our particular fluorescence imaging technique.

Additionally, once the accuracy of the imaging method has been confirmed, we wish to demonstrate our ability to make measurements of atomic currents. Pump-probe spectroscopy only allows for indirect information about the behavior of atoms within a lattice along the symmetry axes, while taking more direct data of atomic current makes it significantly more simple to characterize the observed phenomena of light matter interaction. Section 3.1.2 describes the perturbed MOT experiment, a method of displacing the MOT relative to its equilibrium point. This experiment ensures that our home-built imaging system is capable of tracking center-of-mass motion of the cold atom cloud.

We will show in this thesis the measurement of both diffusive and center of mass motion of an atomic cloud when subjected to a variety of different optical systems. By collecting and analyzing this behavior, we demonstrate reproducible and expected results from imaging techniques. This is a necessary foundation to support any future work using these data collection methods, and we prove the ability to make measurements on the same scale as will be used for the ratcheting experiments

discussed in Section 5.2.

1.3 Previous Work

As mentioned in the previous section, the first objective of this work is to produce results that are externally verifiable by work performed by other groups. Diffusion data of ^{85}Rb in 3D molasses is compared to work done by NIST in 1995 [7]. The work done in optical lattices is designed to allow for comparisons to be made to work done at the University of London by the Renzoni group [8, 9]. Measurements of atomic current use diffusion and damping coefficient values from [10] as a comparison.

The future work, and primary motivation behind the extensive work performed to solidify imaging techniques in our lab, is that of the 2D rocking ratchet, which was briefly introduced at the end of [9]. Theoretical work performed in [3] provides the groundwork for the planned focus of the development of this 2D ratchet into one with precise control of the direction of atomic current in a 2D system.

Chapter 2

Background

In this chapter, I introduce a few core concepts that are the focus of this thesis. First, we introduce the different optical lattice geometries used in this thesis, with a focus on the advantages and disadvantages of each that led to their use for each application. Next, I go into more detail about the two data collection methods, pump-probe spectroscopy and fluorescence imaging, and their different capabilities.

2.1 Optical Lattices

The concept of an optical lattice is one that has been used in the field of atomic, molecular, and optical physics (AMO) for a variety of applications [11]. An optical lattice is a periodic array of potential wells formed by the interaction of several laser beams. During the course of my thesis research, we utilized several different lattice geometries, each of which have different advantages and disadvantages that led to their being used for a particular task. In this section, I will discuss each one in turn, discussing both their experimental geometry, as well as the properties of each that guided our decision in utilizing each one.

2.1.1 3D Tetrahedral Lattice

The tetrahedral lattice, which we also refer to as a lin-perp-lin lattice, is created by four linearly polarized laser beams, the geometries of which are shown in Figure 2.1.

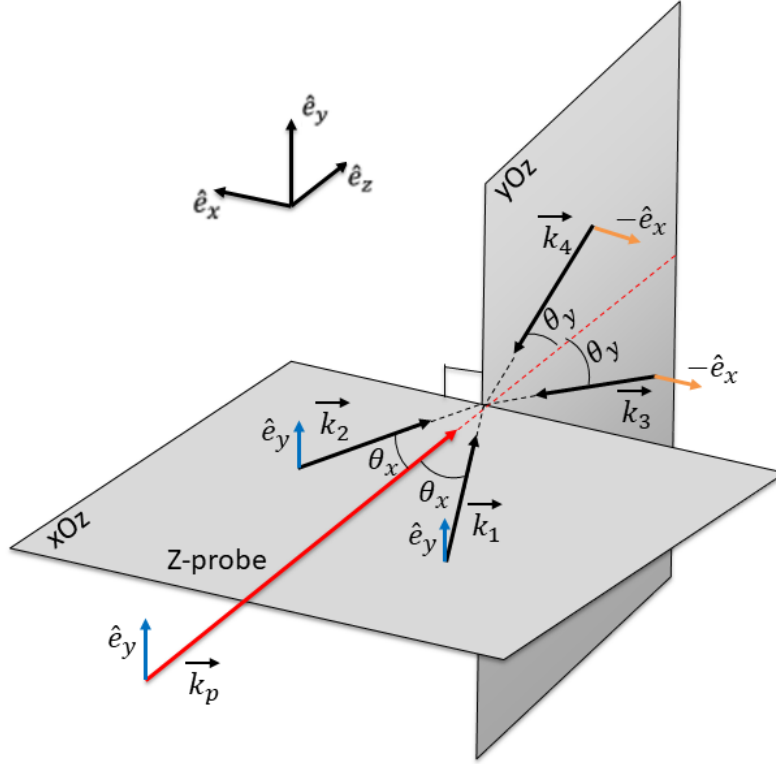


Figure 2.1: Geometry of the 3D Tetrahedral Lattice, with the probe beam included in z as \vec{k}_p . The lattice beams are labelled as $\vec{k}_1 \rightarrow \vec{k}_4$, with polarization unit vectors labelled as e . $\theta_x = \theta_y \simeq 25^\circ$.

At the point where the lattice beams, labeled k_1 through k_4 intersect, there is a 3D interference pattern of alternating areas of linearly and circularly polarized light, creating a series of potential wells. These wells, in the $y = z = 0$ plane, follow a ground state potential given by

$$U_{\pm}(x) = \frac{U_0}{4} [-3 - \cos(2k_x x) \pm 2 \cos(k_x x)] \quad (2.1)$$

The depth of these wells goes as a function of the lattice beam detuning, that is, $U_0 = -16\hbar\Delta'_0/3$. Here, Δ'_0 is the light-shift per lattice field, which goes as $\Delta'_0 \propto I/\Delta$, where I is the intensity per lattice beam, and Δ is the laser detuning. As such, we are able to experimentally alter the features of the lattice through externally controllable variables such as intensity and detuning.

This landscape proves to be an ideal environment for studying the motion of atoms trapped in the lattice that have been cooled through a combination of Doppler and Sisyphus cooling to tens of μK . In this system, the well depth is proportional to I/Δ , while the noise scattering rate is proportional to I/Δ^2 , allowing for these two parameters to be adjusted somewhat independently of each other, a necessary condition for our previous work in stochastic resonance [1]. For these reasons, this is the only lattice used thus far by our lab, as it was ideal for stochastic resonance research, and sufficient for other experiments performed. However, ratcheting experiments done in this lattice use the presence of the probe beam to induce the modulation terms required to achieve a directed atomic current. Since the goal of this thesis is to eliminate the need for the probe beam as a data collection tool, it is useful as well to use a lattice geometry that can achieve ratcheting without the presence of the probe. For this reason, and to draw comparisons with the work done in [8], we use an alternate lattice geometry for the majority of the work done in this thesis.

2.1.2 3D Inverted Umbrella Lattice

The primary lattice configuration used in this thesis is that of the 3D Inverted Umbrella Lattice. The geometry of this lattice can be seen in Figure 2.2. It consists of a single beam on one side of the cloud collinear with the z -axis, referred to as the axial beam, and three beams on the opposite side set equidistant from each other, referred to as the umbrella beams. These umbrella beams are offset from the z -axis by an angle θ . The value for θ is somewhat variable, but due to experimental constraints, we set it to 25 degrees for the entirety of this thesis. The intensities of these beams are more complicated than those of the tetrahedral lattice, due to the uneven symmetry of the beams. It is desired that the intensities be set such that the components of the beams along any one axis comes to a net zero. Referring to [8], we take the relative intensities as $I_1 = 1$, $I_2 = I_3 = \sqrt{3 + \cos^2 \theta}/6 \cos \theta$, and $I_4 = 1/3$. The polarization of the axial beam is linear in x , while

each of the umbrella beams has a linear polarization set along the tangential path of the beams, as seen in Figure 2.2.

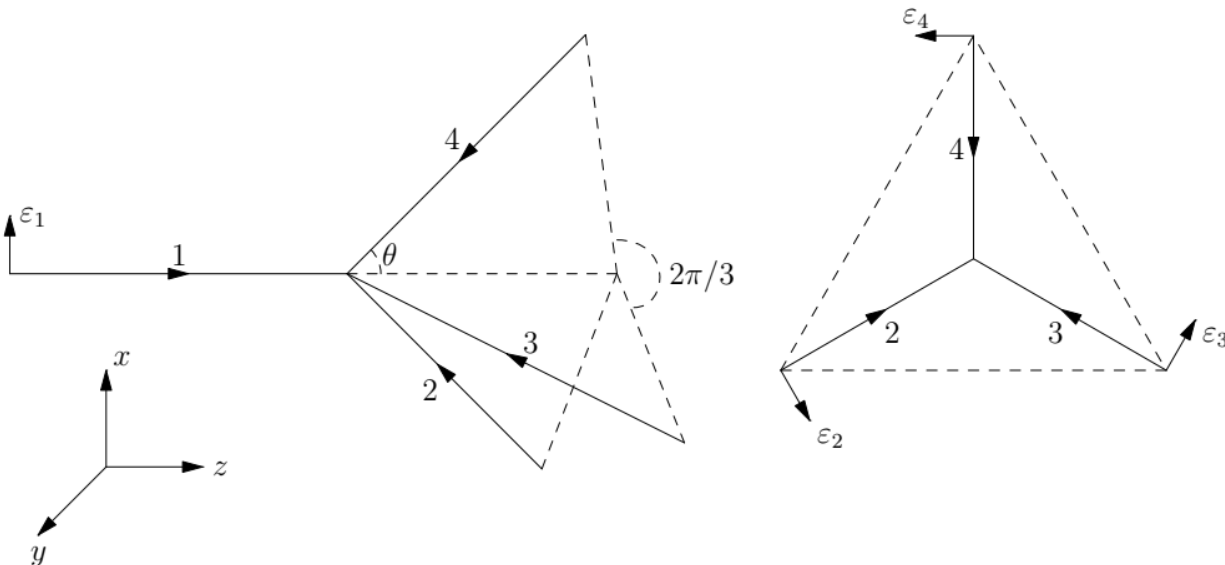


Figure 2.2: Geometry of the 3D Inverted Umbrella Lattice. The lattice beams are labelled $1 \rightarrow 4$, with the polarizations marked as $\epsilon_1 \rightarrow \epsilon_4$. In our experiment, $\theta = 25^\circ$. The right image is a projection onto the xy plane. Image taken from [8].

This lattice has a distinct advantage over the tetrahedral lattice when it comes to ratcheting mechanisms. Unlike the tetrahedral lattice, the presence of the axial beam allows for modulations to be induced in the lattice by frequency driving a single lattice beam. The simple symmetry over the xy -plane significantly reduces the complications in the analysis of this method. It is also possible to take pump-probe measurements in this configuration without the probe creating any significant interference terms, again due to the fact that the axial beam is collinear to the z -axis. In our experiment, a probe beam was added to the configuration co-propagating with the axial beam, but with an $\sim 4.5^\circ$ angle offset towards the $+x$ direction. Due to Doppler broadening effects, the interference term between the probe and the counter-propagating umbrella beams does not produce a significant contribution to the behavior of the atoms, and the very small vector difference between the probe and the axial beam reduces the interference term between them below any significant

levels as well.

The primary reason for using this lattice is the simplicity in moving between ratcheting and non-ratcheting measurements, allowing for the collection of diffusion, temperature, and atomic current data. Additionally, the ability to use pump-probe spectroscopy, even to a limited extent, as well as diffusion imaging allows for an easier transition from a more familiar to a relatively new data collection technique within the context of our lab. This is also the configuration used by the Renzoni group [8], so comparisons can be drawn between our data points and theirs more easily. This lattice is, like the tetrahedral, 3D, so any 2D motion would be over-complicated by symmetry constraints, but for the purpose of developing and testing fluorescence imaging techniques, it is ideal.

2.2 Data Collection Methods

In this section, I will introduce the two methods utilized for data collection in this thesis. While pump-probe spectroscopy has been the dominant form of measurement in the past for our lab, there has been an interest in utilizing fluorescence imaging to supplement our data collection, as well as allow for some measurements that pump-probe is unable to perform [12]. Here, we will cover the theoretical basis that allows these two measurement methods to work, what information can be drawn from the data collected, and the limitations to each one.

2.2.1 Pump-Probe Spectroscopy

Pump-probe spectroscopy is a commonly used technique in the field of atomic, molecular, and optical physics (AMO) [13, 14]. It consists of allowing two beams, a pump and a probe, to interact with each other, while plotting the intensity spectrum of the probe beam as a function of the relative detuning between the two beams. At certain detunings, characteristic peaks and troughs are observed in the transmission spectrum that are indicative of photon transfer between the two beams. By observing the location and amplitude of these peaks, information can be gathered on the behavior of the atoms being illuminated by the two beams. In our case, the lattice beams function as

the pump, while an additional weak beam (less than one percent of the lattice beams) is introduced to the setup to serve as the probe. Additionally, in the tetrahedral lattice geometry, the probe beam introduces an interference term that is essential to the ratcheting process previously studied by this group [1]. In the inverted umbrella lattice, however, the separation between the probe beam and co-propagating lattice beam is greatly reduced, so the modulation caused by the interaction between the lattice and the probe beams in this setup does not create a significant impact on the behavior of the atoms while in the lattice. In a two dimensional lattice, the probe beam is omitted entirely.

The main drawback of the pump-probe spectroscopy method is that this system of data collection can only observe features along a single dimension. Since the spectrum will display a feature when a photon is transferred between beams through an energy level transition of an atom, we can study the transition term between the $|n\rangle$ and $|n + 1\rangle$ energy levels to understand why this is. The transition term will go as follows,

$$\langle n + 1 | \vec{E} \cdot \vec{E}_p^* | n \rangle = \int_{-L/2}^{L/2} \phi_{n+1}^*(x) (\vec{E} \cdot \vec{E}_p^*) \phi_n(x) dx \quad (2.2)$$

where the \vec{E} and \vec{E}_p^* terms represent the lattice and probe fields, respectively. Since adjacent vibrational levels have opposite parity, the $n + 1$ and n terms will always combine to be an odd function. Therefore, this equation is only non-zero if the interference term is also odd. Analysis of the interference term reveals that there is only an odd term along one axis [5], limiting pump-probe analysis to measuring one dimensional motion exclusively. In the three dimensional lattice, this was acceptable as the ratcheting being studied was one dimensional, but when moving to a two dimensional lattice with two dimensional ratcheting, it proves to be insufficient. Additionally, since the probe is not used directly to induce the ratcheting in the inverted umbrella and two dimensional lattices, in a system where it is not being used for data collection it becomes unnecessary to include one at all.

2.2.2 Fluorescence Imaging

Fluorescence imaging is, at a base level, much simpler than pump-probe spectroscopy. The basic idea is that a camera is pointed at the cloud, and pictures are taken at specific time intervals in order to study the behavior of the cloud over time. Precise analysis of these images allows for the extraction of the full width half maximum (FWHM) of the cloud and the relative motion of the center of mass. However, since the time and distance scales over which these measurements are taken are on such a small order of magnitude (milliseconds and millimeters), it can be difficult to experimentally implement a system while maintaining a reasonable budget. Additionally, the light from the cloud that needs to be captured is extremely weak, requiring a highly sensitive camera.

The sensitivity requirements can be satisfied by using a camera designed for astronomical photography, but these cameras are designed for long exposure times without the need for millisecond level precision. To circumvent this limitation, we use a resonant imaging beam that can be pulsed on by an AOM more precisely than the camera. While the camera's exposure and capture timing cannot be set directly to the single millisecond level, an AOM can be pulsed on for a single millisecond, while knowing the exact millisecond at which that occurs. By setting the exposure time of the camera to a longer window (in our case 7ms), and ensuring the only lasers active during that exposure window is the imaging pulse, we can effectively take a single millisecond exposure time as there is no fluorescence to be captured during the remaining time the camera shutter is open. This process is discussed in more detail in [15]. To further the accuracy of this method, a background image is captured in addition to the main image for every data point, by repeating the experiment but with the imaging beam mechanically blocked. Subtracting this background image ensures that the data being saved and analyzed is only the contribution made by the fluorescence caused by the imaging beam pulse. An example of this process is found in Figure 2.3. Chapter 3 discusses the experimental implementation and timing control of fluorescence imaging in more detail.

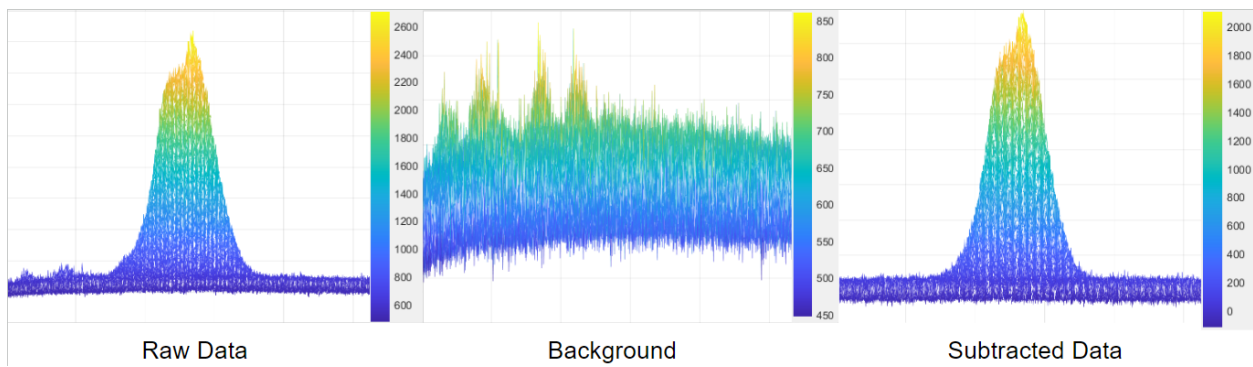


Figure 2.3: Data collected by the imaging system. On the left, we have the raw data taken by one experimental cycle. The middle shows background data collected by repeating this process, but with the imaging beam blocked. The right graph is created by subtracting the background from the raw data. The left and right graphs are scaled the same, while the y-axis on the background image is zoomed in to show detail.

Chapter 3

Experimental Procedure

In this chapter I describe the experimental procedure in more detail. It is organized by splitting the experiments performed in the MOT and molasses from those performed in a 3D lattice. We focus on the hardware used to create these optical systems, as well as the software used to control the high precision timing cycles required. The end of the chapter also includes some miscellaneous experimental techniques that were broadly applied to this work at large.

3.1 MOT and Molasses

A MOT, or magneto-optical trap, is a system frequently used in optical physics to study light-matter interaction. Our system utilizes a MOT of ^{85}Rb , with the trapping lasers operating from the $F_g = 3 \rightarrow F_e = 4$ transition cooling and trapping atoms within a vacuum chamber with pressure lowered to $\sim 10^{-10}$ Torr. Additionally, a repumping beam is used to excite atoms out of $F_g = 2$ in order to avoid a loss of trapped atoms as they fall into that state. In a standard MOT, a magnetic gradient is used to cause the atoms to congregate in the center of the vacuum chamber, where they encounter the cooling beams. Molasses refers to a system where the magnetic gradient has been deactivated, allowing the atoms to gradually diffuse against the retarding force of the cooling beams. In this section, we use our imaging system to observe the motion of the atoms in the MOT and the molasses, and from this motion extract information about the diffusion constant and temperature.

3.1.1 Diffusion Constant and Temperature in Molasses

The first data points we collected were diffusion measurements of atoms in molasses. When atoms are freed from the trapping force of the magnetic gradient in the MOT, they diffuse randomly in all directions, but are still constrained by the cooling beams. By varying the amount of time that the atoms are allowed to expand in this molasses, it is possible to extract useful data from their acceleration. Most notably, the diffusion constant can be extracted from this data [7], and the relative simplicity of this experiment is a good first check of the performance and sensitivity capabilities of our imaging system. We begin by taking a series of images with different timing sequences, which is discussed in more detail below. Once the images have been captured, they are run through MATLAB code (see Appendix B) that fits a full width half maximum (FWHM) to the data and calculates the relative areas of the cloud, using a Gaussian fit.

The diffusion constant was calculated using the area of the cloud as it expands, as was done in [7]. For each data point, the area was collected in the following manner. First, following [7], we define three ratios β as $1/3$, $1/2$, and $2/3$. For each value of β , we determine the intensity value that corresponds to that much of the total intensity. A visual of this can be seen in Figure 4.2. Then each pixel that has an intensity larger than that value is summed together, and using the pixel to cm conversions determined in section 3.3.1, converted to an area in units of cm^2 , A_β . Since there are three values of β , we get three values for area that are later averaged. A diffusion constant can be extracted from each using the following equation taken from [7]:

$$A_\beta = 4\pi t D_x \ln(\beta^{-1}) \quad (3.1)$$

Temperature measurements can be extracted very similarly. For the case of temperature data, we are interested in how the atoms expand when they are experiencing no optical forces at all. By measuring their expansion as a rate of time, we can back out an average velocity and convert that to temperature. We do this by keeping a constant molasses time, but adding an additional time period where we turn off the cooling beams as well and allow the atoms to expand freely. We call this time ballistic expansion time. Using the same MATLAB programs as in the diffusion data, we can find the FWHM of the cloud at different ballistic expansion times. The equipartition theorem gives

us $\frac{1}{2}k_B T = \frac{1}{2}mv^2$. If we allow half the FWHM to represent the relative position of an expanding atom, we get:

$$v_x = \frac{dx}{dt} = \frac{1}{2} \frac{d}{dt}(FWHM_x) \quad (3.2)$$

and from the equipartition theorem:

$$T_x = \frac{mv_x^2}{k_B} = \frac{m}{k_B} \left(\frac{1}{2} \frac{d}{dt} FWHM_x \right)^2 \quad (3.3)$$

giving us a direct relation to temperature from the slope of a graph of the FWHM/2 against ballistic expansion time.

The experimental timing cycle for these measurements is controlled by a LabVIEW program created by the Miami Instrumentation Lab. A sample timing sequence for MOT data collection can be found in Figure 3.1. The first line is the line controlling the coils for the magnetic gradient of the MOT. These coils are turned off at 1 second, which forms the relative start point for all other lines. After the coils turn off, we first wait a minimum of 2.5ms for eddy currents to die away in the coils, and an additional 1ms for thermalization time in the molasses, for a combined 3.5ms gap. It is worth noting that waiting additional time is not an issue outside of a gradual loss of signal, which is why many older timing sequences wait 4.5ms to ensure thermalization has definitely completed. In our case, after the 3.5ms gap, we define that point as $t = 0$. From there, we wait a variable amount of time that we call molasses time. For diffusion measurements in molasses, this is the changing variable of interest.

In Figure 3.1, the molasses time is 40ms, but for the data presented in this thesis it varies between 2.5 and 250 milliseconds. The trap is then switched off, along with the repump. We then wait another variable amount of time that we refer to as ballistic expansion time. Due to the jitter in the camera exposure window [15], the ballistic expansion time must not be less than 6ms. When taking temperature measurements in both molasses and the lattice, this is the changing variable of interest.

After the ballistic expansion time, the repump and imaging beams are both flashed on for 1ms to cause the fluorescence that is captured by the camera. After some time, a minimum of 6ms due

to the exposure jitter, the MOT beams are turned back on to allow the MOT to load for the next cycle. The final line, the camera, is set so that it activates precisely 237ms before the imaging pulse starts, due to a delay between the camera receiving the capture signal and actually beginning exposure [15]. This entire cycle is typically repeated approximately ten times to collect a sample of images to be averaged, and another five times with the imaging beam mechanically blocked to collect a sample of background data.

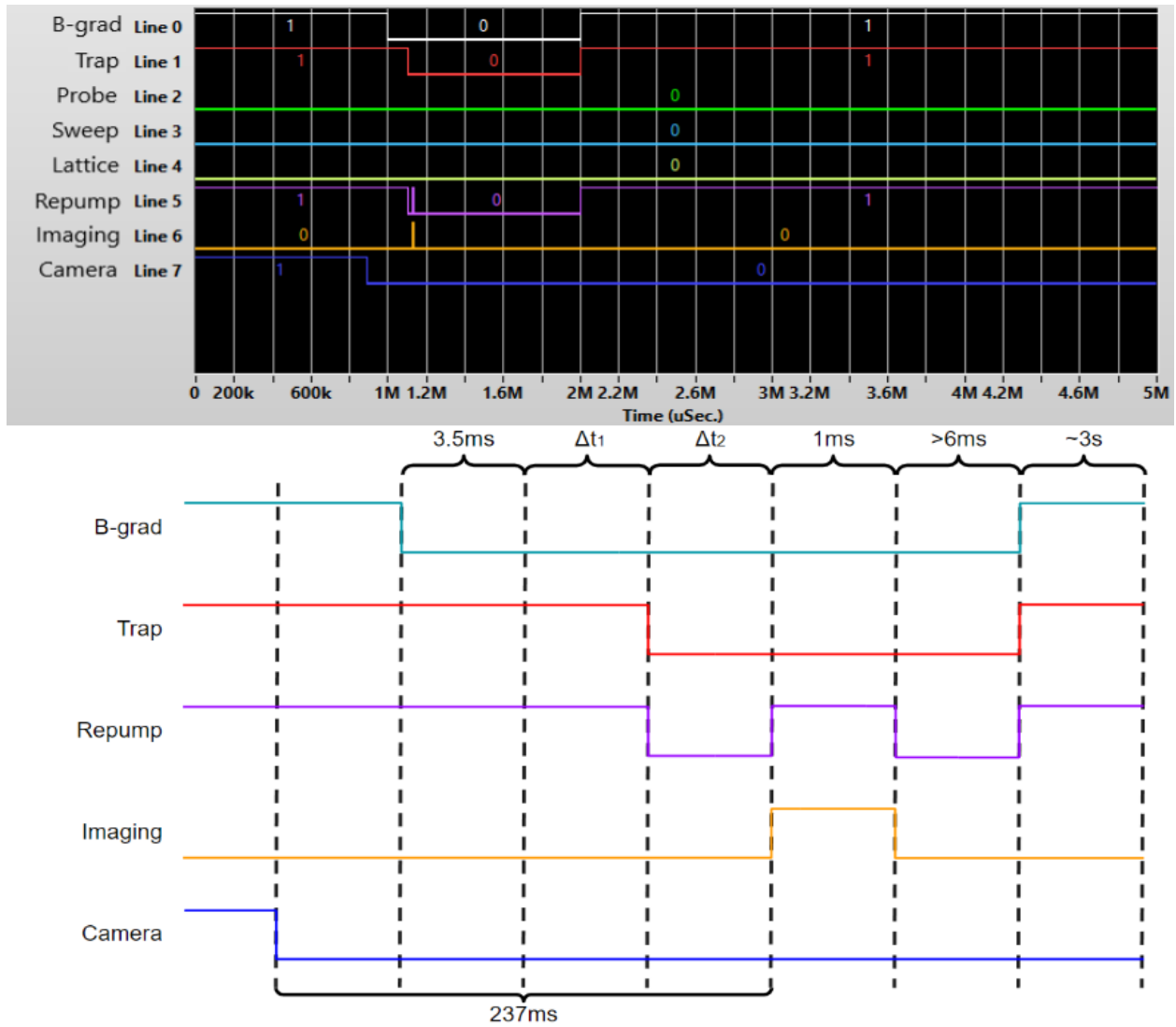


Figure 3.1: Full timing diagram for a molasses diffusion imaging cycle. The top figure shows the LabVIEW display for 100ms molasses time and 30ms ballistic expansion time. The bottom figure shows the sequence in more detail. Δt_1 is the molasses time, and Δt_2 is the ballistic expansion time. Note the camera triggers on a falling edge.

3.1.2 Perturbed MOT

After completion of the diffusion and temperature measurements, we want to establish the ability of our imaging system to measure atomic current through detection of center of mass motion. The perturbed MOT experiment, based on work done in [10], accomplishes this goal. The basic concept of this experiment is to observe the restorative motion of the MOT after being displaced by a biased magnetic field. In our setup, this is accomplished by switching on a Helmholtz coil with a previously set current. This causes the magnetic fields to be stronger from this direction, and the MOT moves to a new equilibrium point, offset from the original location on the scale of a millimeter or less. The magnetic field is then switched off, restoring the equilibrium point to the center of the gradient. This results in a system not unlike that of a simple harmonic oscillator, where the cloud has been given a certain displacement, and there is a position dependent restoring force trying to bring it back to equilibrium, working against the retarding force of the cooling beams. By taking images of the cloud at specific time intervals, we can plot the center of mass motion of the cloud as a function of time. This behavior can be analyzed to extract a diffusion constant, the values of which should agree with those found using the direct diffusion imaging method. The timing diagram for this experiment can be seen in Figure 3.2.

For this experiment, the magnetic gradient does not need to be switched on and off as it was for previous experimental cycles. Instead, the $-z$ Helmholtz coil needs to be switched on and off in sync with the rest of the timing cycle. Therefore, the $-z$ Helmholtz coil needed to be rewired to a power supply that is connected to a switch in communication with LabVIEW. There was an additional complication in that the gradient supply and the $-z$ supply use different connections. However, the power supply that was being used for the rubidium getters is capable of being wired to the switch and has the same connection type as the $-z$ supply. Therefore, it was experimentally easier to transfer the high voltage switch connection to the former power supply for the Rubidium getters from the gradient coil, and then switch the Rubidium getter and $-z$ Helmholtz connections.

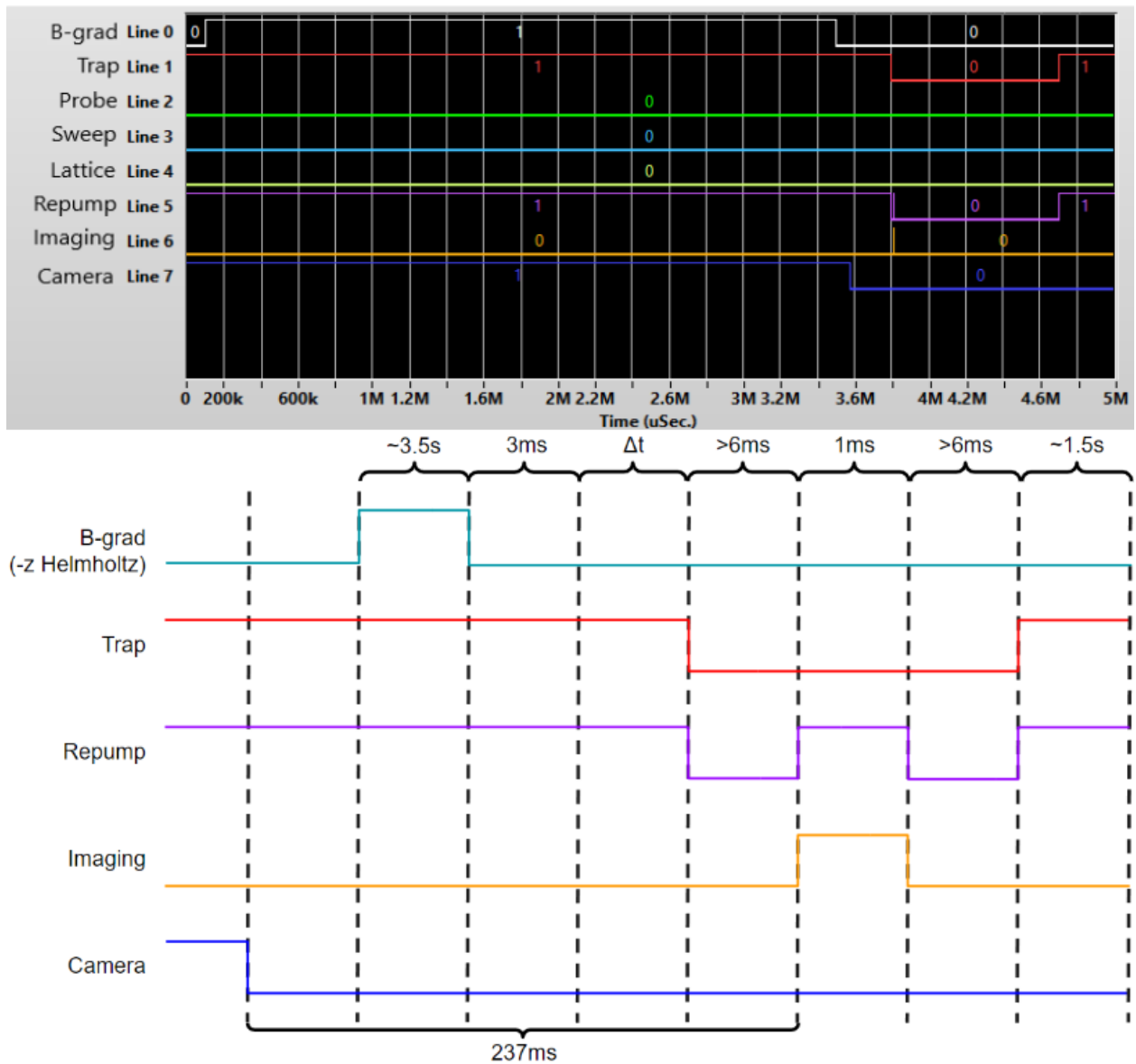


Figure 3.2: Full timing diagram for the perturbed MOT experiment. For this experiment, the B-grad line was rewired to the $-z$ Helmholtz coil. The top figure shows the LabVIEW display, and the bottom figure shows the sequence in more detail.

3.2 3D Lattice

In this section, I discuss the work done in an optical lattice. We start by covering some of the initial work done with pump-probe spectroscopy used to detect the successful formation of the lattice. Next, we discuss the diffusion and temperature measurements performed in the lattice, with a focus on the differences between these measurements and those done in molasses. Last, we cover the 3D ratchet experiment that was performed to detect atomic current in the lattice.

3.2.1 Pump-Probe Spectroscopy

As discussed in subsection 2.2.1, pump-probe spectroscopy has certain limits when being applied to multi-dimensional signals. However, since it was commonly used for experiments previously done by this group [1], it serves as a good initial check to ensure the new lattice geometry is forming as expected. While previous experiments used a probe beam for both modulation effects as well as data collection, the umbrella lattice is modulated by direct frequency modulation of the axial beam. Because of this, we want the probe beam for the umbrella lattice to be as closely collinear to any co-propagating beams as possible, to reduce the impact of the interference term on atomic behavior. It makes sense, then, to bring the probe beam in from the same direction as the axial beam, so that any interaction it has with the three umbrella beams is made negligible by Doppler broadening. Experimentally, it is impossible for the probe to completely overlap with the axial lattice beam and then be separated after the chamber as they have the same polarization, but a small angle of displacement will not create any significant effect on the same scale as the lattice modulation. Figure 3.3 shows the geometry of the umbrella lattice with the probe beam included.

Once the probe beam has been added to the system, it is a simple matter to perform a pump-probe spectroscopy measurement for a series of different lattice beam intensities and detunings. While performing these measurements, we can ensure that the lattice is successfully forming by collecting spectra with and without the lattice beams mechanically blocked, and comparing the results. These spectra are shown and discussed in chapter 4.

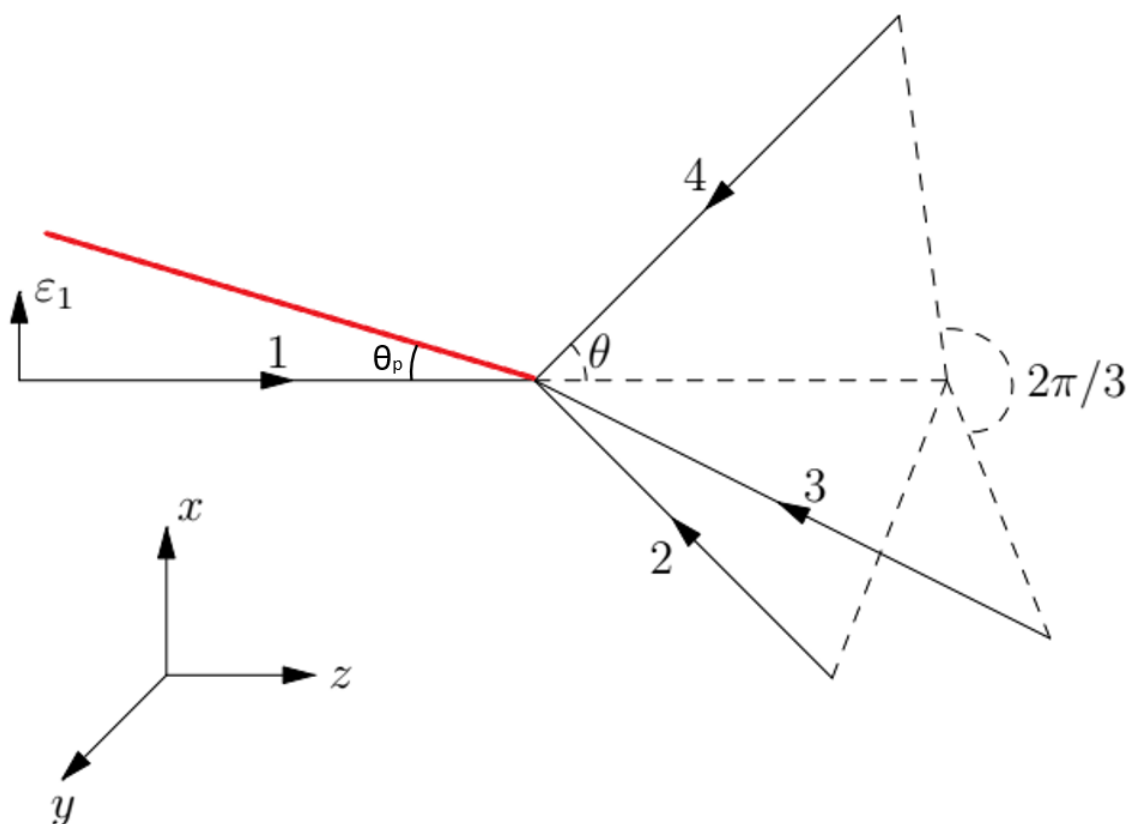


Figure 3.3: Geometry of probe beam for the umbrella lattice. The probe, in red, lies along the xz -plane. In our system, $\theta_p \approx 4.55^\circ$. Figure adapted from [8].

3.2.2 Diffusion Constant and Temperature in 3D Lattice

Once it has been established that the inverted umbrella lattice is forming, we can use fluorescence imaging to gather information about this lattice geometry, namely the diffusion constant and temperature of the atoms when fully thermalized in the lattice. This is done almost identically to how diffusion and temperature data is taken in molasses, but instead of molasses time with no trapping forces but the trap beams, the only constraining force is the lattice. The timing diagram for these experiments is shown in Figure 3.4. The main difference is the presence of the lattice beams, line 4. Where before there was a period of time with only trap beams present, now the duration of the lattice pulse is the time of interest for diffusion measurements. Like discussed in section

3.1.1, there is a 3.5 ms gap after the B-gradient is turned off, but after that gap, the trap beams are switched off and the lattice beams are switched on simultaneously. We then wait an amount of time which we refer to as lattice diffusion time, after which the lattice and repump beams are turned off. Again, at least 6 ms of ballistic expansion time is necessary before the imaging pulse is triggered. Using Equation 3.1, the diffusion constant can be extracted from a graph of the cloud area against lattice diffusion time.

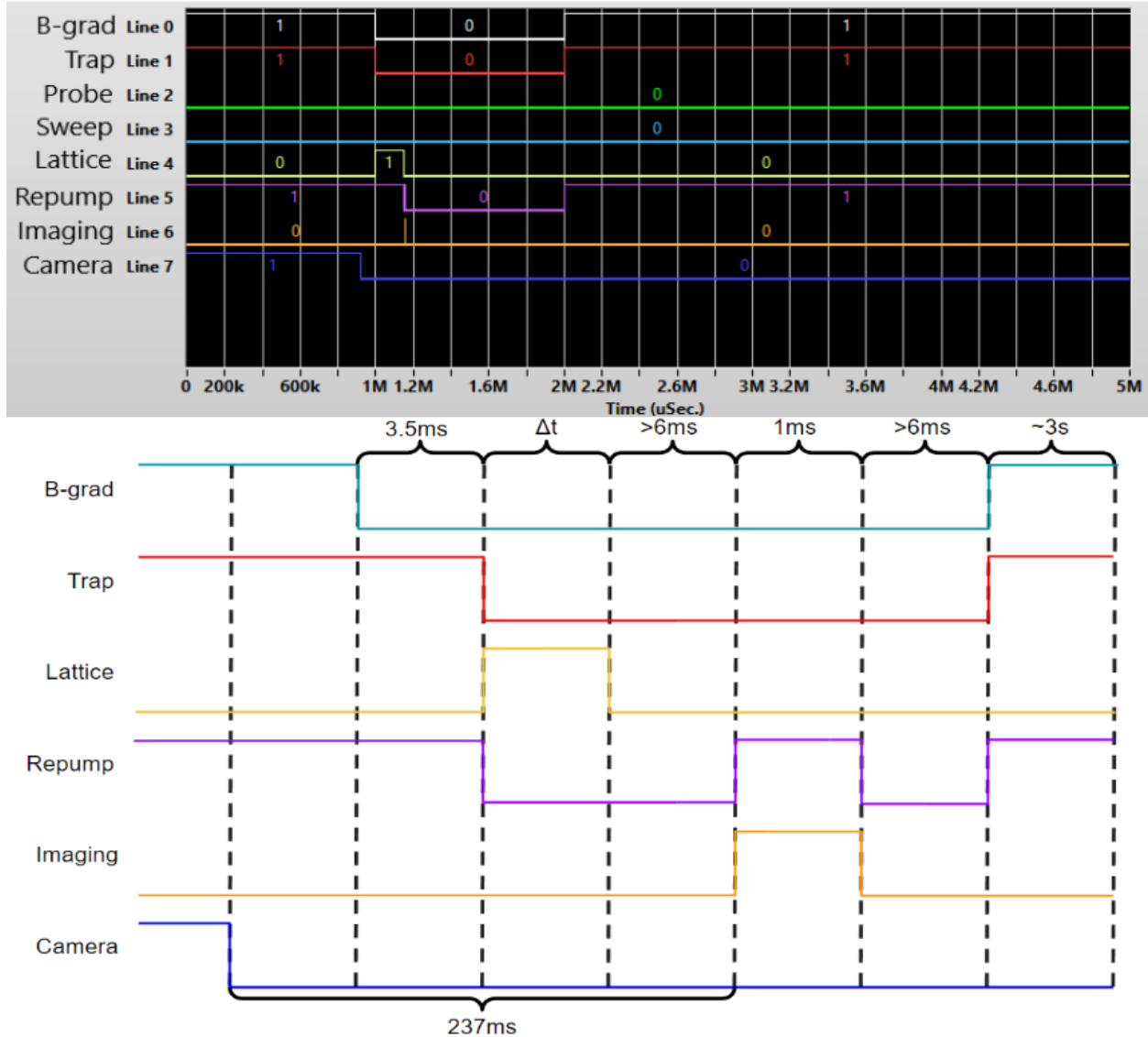


Figure 3.4: Full timing diagram for a lattice diffusion imaging cycle. The top figure shows the LabVIEW display, and the bottom figure shows the sequence in more detail.

Temperature measurements are made by holding the lattice diffusion time constant, and changing the ballistic expansion time. Initially, measurements were taken at 10, 20, 50, and 100 ms of lattice diffusion time, but after observing a lack of significant difference in the temperature measurements at each of these values, later experimental cycles take fewer data points, as it is clear that the lattice has thermalized sufficiently by 10 ms at most. In fact, a thermalization time of 2 ms was found by this group previously [5], but since the signal is still very clear after longer lattice diffusion times, we often used 50 ms to allow for a larger sized cloud when the images are taken. The temperature measurements themselves use Equations 3.2 and 3.3, and plotting half the FWHM against ballistic expansion time lets a temperature be extracted.

3.3 Additional Experimental Techniques

This section details a few miscellaneous experimental techniques that were used broadly in all data collection. Namely, we discuss how the values for pixel-to-centimeter conversion for the fluorescence imaging was determined, as well as how atom counts are taken accurately for each experiment.

3.3.1 Pixel to Centimeter Conversions

As another consequence to the altered collection methods of the LabVIEW program, it is necessary to recalculate the pixel-to-centimeter conversion for our camera system. While this has been done before by our group [6], these conversion factors are no longer valid since we no longer perform the same binning reductions to the incoming data. In order to find the new conversion factor, we simply took an image of a ruler with the lens system carefully replicated away from the vacuum chamber. Figure 3.5 shows the setup utilized for this process, which is also the lens system used for the diffusion imaging. In our setup, we utilize two inch $f = 170\text{mm}$ lenses plano-convex lenses. It is imperative that the distances f are as precise as possible, since even small variations can cause significant impact when measuring at such a fine scale. By capturing an image of a ruler, it is a simple process to measure the pixels between the ticks on the ruler using the LabVIEW program.

We found that 3 mm corresponded to 710 pixels, for a conversion factor of 4.23×10^{-4} cm/pixel, for a binning level of one (no binning).

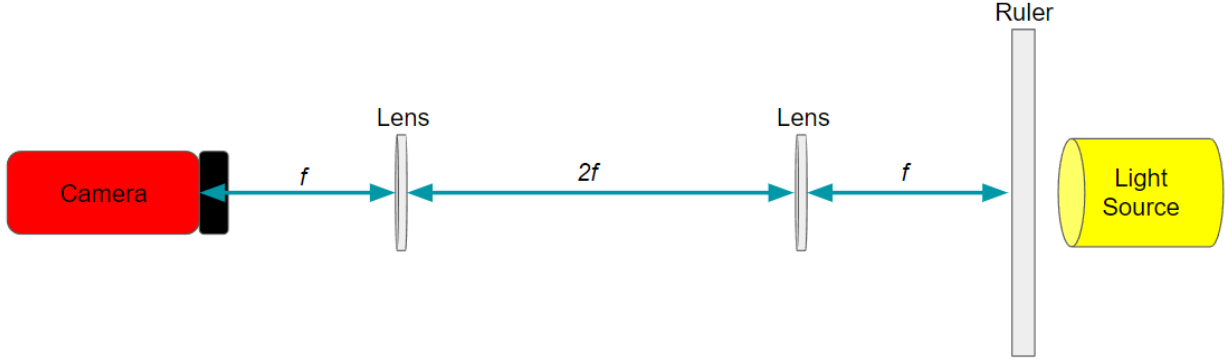


Figure 3.5: Diagram demonstrating the setup used to determine pixel to centimeter conversion rates. The two lenses should have equal focal length. Note that the length f between the camera and the leftmost lens must extend to the photodiode of the camera, which is distinct from the front of the camera mount.

3.3.2 Fluorescence Imaging for MOT Atom Count

A similar, but notably simpler system is utilized for determining the number of atoms trapped within the MOT at any given time. Utilizing a photodiode and current to voltage converter, the amount of light being emitted by the cloud is displayed as a voltage signal on an oscilloscope. While this signal can be used fairly directly when considering relative atom counts (that is, if you want the same number of atoms over several experimental cycles, you can just ensure the voltage signal is the same for each cycle), it takes some brief calculations to extract an exact atom number from the displayed voltage, given by the following equation taken from [5].

$$N \times \hbar\omega_0 \times \frac{1}{\tau} \times \rho_{ee} \times \frac{\Omega}{4\pi} \times L \times G \times \frac{I}{V} = \text{Signal} \quad (3.4)$$

Chapter 4

Results and Analysis

In this chapter, I present and discuss the results collected from the experiments laid out in Chapter 3. The data is compared to expected outcomes as well as past results from other groups, and any discrepancies are identified and discussed.

4.1 MOT and Molasses

As previously discussed, the most basic check of our fluorescence imaging system is taking measurements of atomic behavior in the MOT itself. Diffusion and temperature data is a simple matter of taking a series of images while the cloud expands, and does not even require center of mass measurements. In section 4.1.1, therefore, we present sample graphs demonstrating how both diffusion and temperature data is calculated, then present a table of the data points that were measured.

In section 4.1.2, I present the data collected from the perturbed MOT experiment. We extract a diffusion constant from this data, and compare the results to those found in 4.1.1.

4.1.1 Diffusion Constant and Temperature in Molasses

We collected data for the diffusion constant in molasses using two different configurations of the trap intensities. The first we refer to as a 40/40/20 split. This configuration has the MOT beams split such that the x and y cooling beams both receive $\sim 40\%$ of the total trap power, while the

z beam receives the remaining 20%. This is the standard trap split for experiments in our lab, since the orientation of our anti-Helmholtz coils along the z -axis results in the magnetic gradient being stronger in that direction by a factor 2. Because of this, the 40/40/20 split results in the most compact, stable cloud, and is ideal for previous work that utilized the MOT only as a starting point to load an optical lattice. However, since the molasses data collected in this section involves switching off the magnetic gradient, the 40/40/20 split resulted in unequal constraining forces along different axes. Thus, we also take data measurements where the trap intensities are equal along each axis, referred to as equal intensity split. For the work done in this thesis, the combined trap power, not including retroreflections, is $\sim 25\text{mW}$.

Figure 4.1 shows a sample plot used for calculating diffusion measurements. As discussed in Chapter 3, the MATLAB code AFinder (see Appendix B) is used to find the area of the cloud that is above $1/3$, $1/2$, and $2/3$ of the maximum value. These different ratios we call β , for easy comparison to data taken from [7]. Figure 4.2 demonstrates the approximate areas each value for β captures. This process of finding the area is discussed in more detail in section 3.1.1.

A linear trendline is added to the data points, using Microsoft Excel's built-in trendline function, and the slope of each line is used with equation 3.1 to calculate a diffusion constant of that data set. Each data set is taken twice, and an average taken, as there is a non-negligible amount of variance to the data caused by slight differences in the experimental system from day to day. Table 4.1 presents the final diffusion constant results for ^{85}Rb in molasses. We compare these values to those found in [10] and [7]. For the value found in [10], which was $(1.01 \pm 0.15) \times 10^{-1}\text{cm}^2/\text{s}$, there is a difference of approximately two orders of magnitude, which we attribute to the difference in MOT parameters between our two systems. For [7], however, a value of $\sim 1.5 \times 10^{-3}\text{cm}^2/\text{s}$ was reported for their data set collected with trap beam intensities and alignments most close to ours, which agrees with our data to less than an order of magnitude.

Next, temperature data was collected in molasses. Here, we set the molasses expansion time to a constant, and vary the ballistic expansion time in an effort to measure the velocity that the atoms were moving at when the trap beams were switched off. While the atoms expand in molasses, there is an amount of time on the scale of milliseconds for the atoms to reach a fully thermalized state.

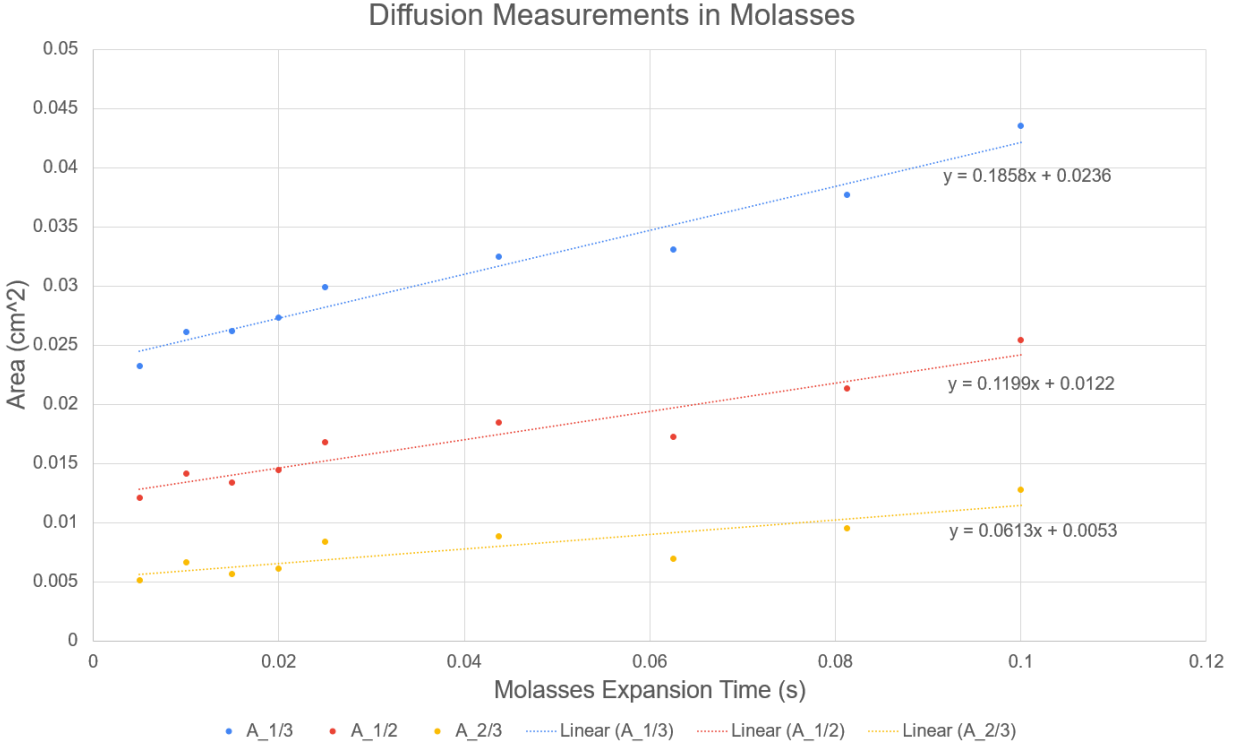


Figure 4.1: Plot of cloud area against molasses expansion time. The trap powers are set to a 40/40/20 relative intensity split, with the 20% corresponding to z .

In an effort to ensure that we have cleared that area of fluctuating temperatures and behavior, we take data at two different molasses expansion times, 10ms and 50ms. We expect, assuming we have cleared the thermalization time sufficiently, very little discrepancy between the temperatures found at these two points. The data also is collected at the 40/40/20 and equal intensity trap splits as it was for diffusion.

Figure 4.3 shows a sample data set for a 10ms molasses time. Similarly to the diffusion data, the slopes of these lines are the meaningful values. For temperature data, they represent the displacement over time of the atoms, which of course can be read as a velocity. Using these slopes and equation 3.3, a temperature can be collected from the graph.

In Figure 4.3, it is clear that there are measurably different slopes along each axis in the image. This is due to the asymmetry in the trap beams, but an average temperature can be extracted from this data that is more representative of the cloud as a whole. While the image captured is 2D, the

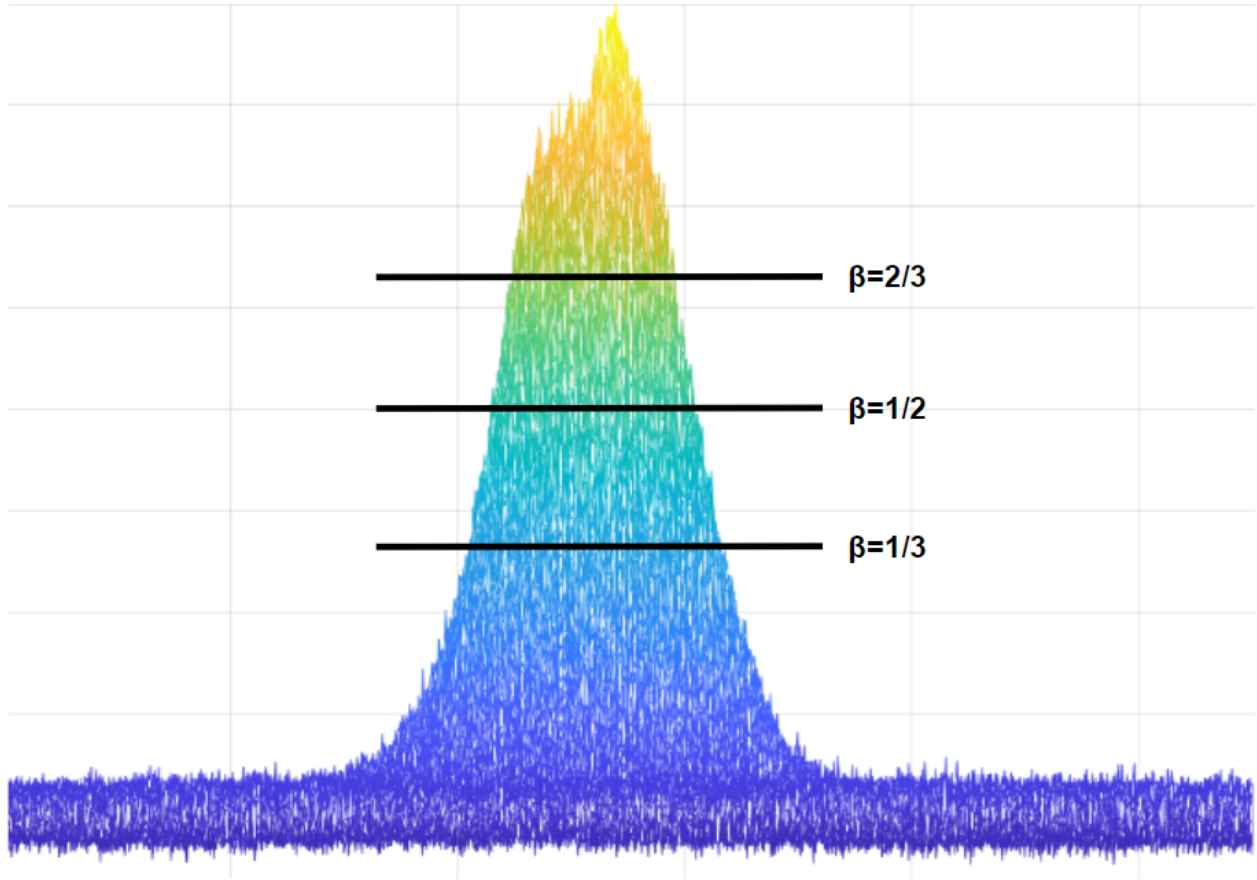


Figure 4.2: Relative locations for each value of β . For each value, the area is taken as the number of pixels above the line.

cloud itself is of course 3D, and this is taken into consideration when the average is calculated. While we only image the x and z axes, the y axis is experimentally identical to the x axis. As such, we expect that the temperature data along y would also be identical to what is found along x . Following this logic, the average temperature was determined using the following equation:

$$T_{avg} = \frac{2T_x + T_z}{3} \quad (4.1)$$

where the temperature in x is weighted twice to account for the temperature in y as well. The temperature data recorded for the different trap splits and different molasses times is recorded in Table 4.2.

Table 4.1: Measured diffusion constants in molasses

Trap Split ($I_x/I_y/I_z$)	β	Average Diffusion Constant (cm^2/s)
40/40/20	1/3	9.9×10^{-3}
40/40/20	1/2	9.1×10^{-3}
40/40/20	2/3	6.4×10^{-3}
Equal	1/3	7.3×10^{-3}
Equal	1/2	6.0×10^{-3}
Equal	2/3	4.3×10^{-3}

Table 4.2: Measured temperature in molasses

Trap Split ($I_x/I_y/I_z$)	Mol. Time (ms)	Avg. Temp (μK)
40/40/20	10	48.0
40/40/20	50	41.9
Equal	10	55.2
Equal	50	54.9

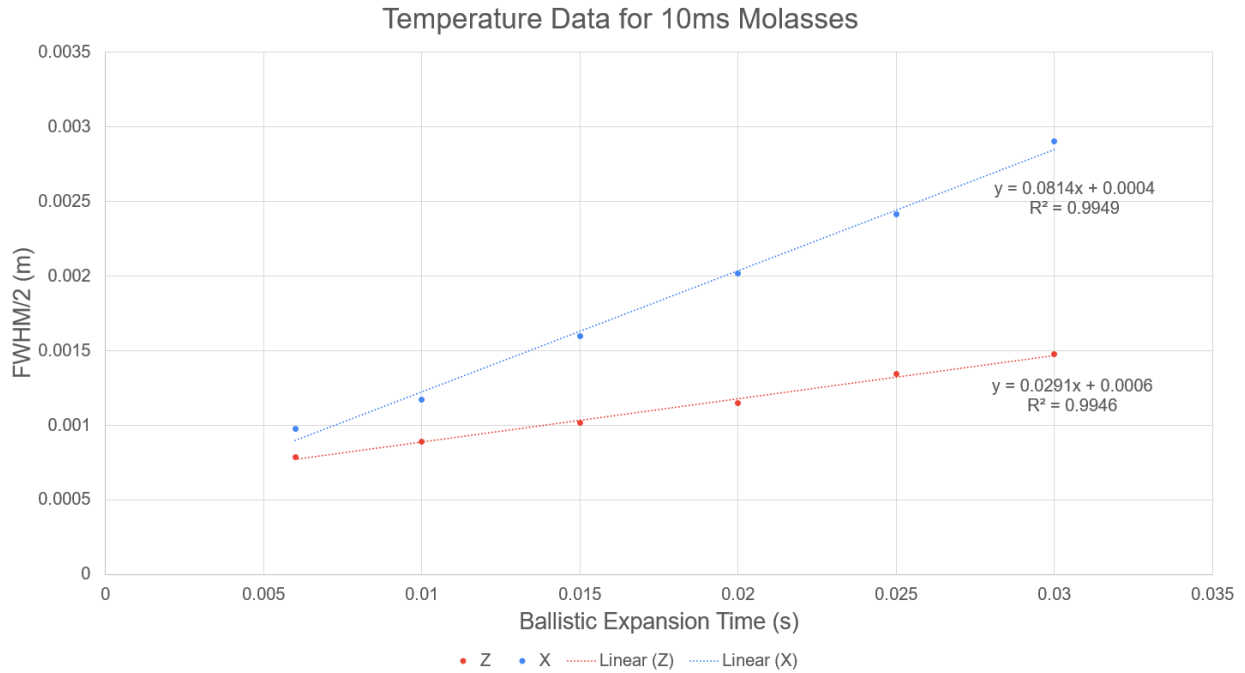


Figure 4.3: Plot of half the full width half max of the cloud against ballistic expansion time, after 10ms of molasses time. The trap powers are set to a 40/40/20 relative intensity split, with the 20% corresponding to z.

4.1.2 Perturbed MOT

The data collected from the perturbed MOT experiment is studied in more detail in [16], but here we compare the calculated values for the damping coefficient, α , to external data found in [10]. The damping coefficient has a direct relation to the diffusion constant, which goes as $D = \frac{k_B T}{\alpha}$. Using the data collected earlier in this section in Table 4.2, the average temperature in our system is $44.933\mu\text{K}$, as the perturbed MOT experiment was done with a 40/40/20 trap split. For the diffusion constant, the average value is $0.00849\text{cm}^2/\text{s}$ from Table 4.1, again using only the 40/40/20 data. This results in a value of $\alpha = 7.303 \times 10^{-22}\text{kg/s}$, which is in reasonable agreement with the values found in [10].

Also found in [10] is a simple theoretical calculation for α of a 1D, 2-level atom. The formula is as follows:

$$\alpha = \frac{8\hbar k^2 \frac{I}{I_s} \frac{\Delta}{\Gamma}}{\left(1 + \frac{I}{I_s} + \frac{4\Delta^2}{\Gamma^2}\right)^2} \quad (4.2)$$

where $k = \frac{2\pi}{\lambda} \approx 0.00805\text{nm}^{-1}$ is the wave number and $\frac{\Delta}{\Gamma} = 3$ is the trap detuning over the natural linewidth. I/I_s is the total trap intensity divided by two over the saturation intensity. Our total intensity for all six trapping beams in our 3D experiment is $7.92\text{mW}/\text{cm}^2$. For a 1D approximation, there are only two trapping beams, so we divide this value by two to get $I = 3.96\text{mW}/\text{cm}^2$. Therefore, with a saturation intensity of $I_s = 1.67\text{mW}/\text{cm}^2$, we have $I/I_s = 2.37$.

Using these values, we get a result of $\alpha = 2.509 \times 10^{-22}\text{kg/s}$, which is not far from the measured value above. Note that our equation corrects an erroneous factor 2 from [10], which comes from the excited state fraction used in the derivation.

4.2 3D Lattice

The data taken in this section was performed in the inverted umbrella lattice detailed in section 2.1.2. First, we perform pump-probe spectroscopy measurements aimed to demonstrate the successful formation of the lattice. Similar to the work done in [1], we expect to observe distinct peaks and troughs at certain frequencies corresponding to the vibrational frequencies within the lattice, and

using their positions and amplitudes, we can ensure our lattice is working as expected. We then perform diffusion and temperature measurements in the inverted umbrella lattice, comparing the results to external work as well as the data collected in molasses. Lastly, we discuss the progress made toward establishing a 1D ratchet in the lattice.

4.2.1 Pump-Probe Spectroscopy

The method of pump-probe spectroscopy is detailed in section 2.2.1. In short, a weak probe beam is used to collect data from the lattice through interaction with the lattice beams. The beam is then run to a photodetector, and the intensity of the beam is plotted as a function of the detuning between the probe and lattice beams. Figure 4.4 shows the unmodified transmission spectrum of our probe beam passing through a lattice with a detuning of 8.75Γ , an axial beam intensity of $16.25\text{mW}/\text{cm}^2$, an intensity of $5.84\text{mW}/\text{cm}^2$ for lattice beams two and three (see Figure 5.1 for beam labels), and an intensity of $5.42\text{mW}/\text{cm}^2$ for lattice beam four.

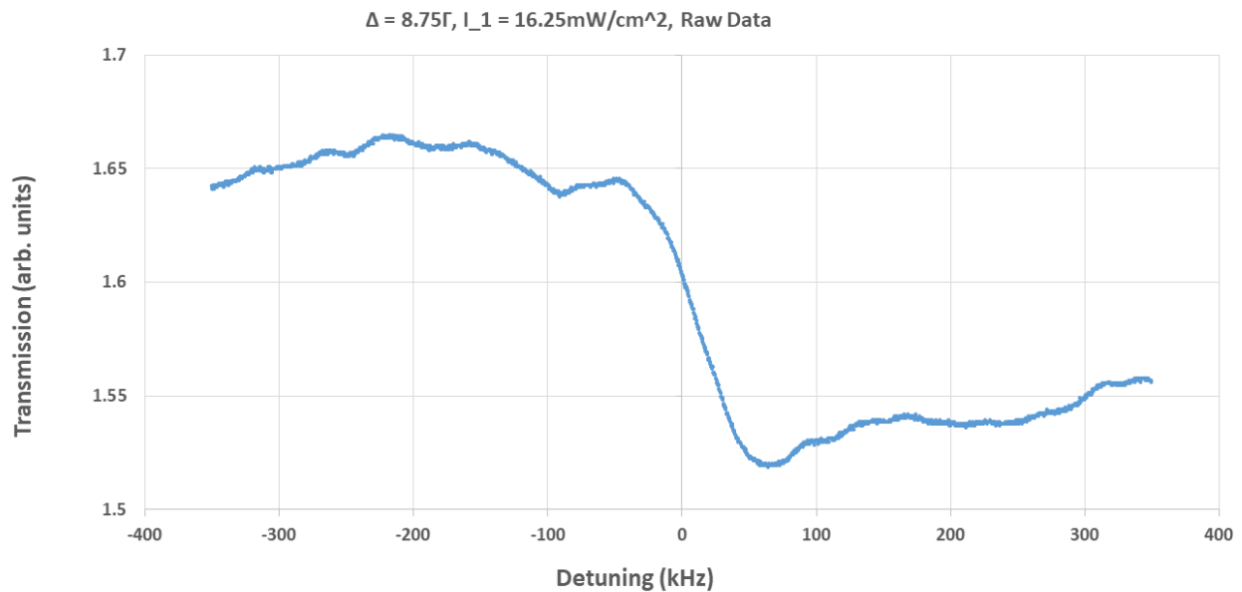


Figure 4.4: Pump-probe spectrum taken in an inverted umbrella lattice at a detuning of 8.75 gamma and $16.25\text{mW}/\text{cm}^2$ axial intensity, $5.84\text{mW}/\text{cm}^2$ beam two and three intensity, and $5.42\text{mW}/\text{cm}^2$ beam four intensity, without any background subtraction.

Additionally, as shown in Figure 4.5, a background spectrum is taken to isolate the signal caused by only the atoms. This is done by turning off the magnetic gradient used in the MOT, and retaking the pump-probe spectrum with no other adjustments. Without the magnetic gradient, the atomic cloud will not form, but since the rest of the system is unaltered, any noise caused by optical elements, reflections, other laser beams, and the like will be recorded. Once the background and raw data are collected, we subtract the background signal from the raw data point by point, yielding only the effects caused directly by the atomic cloud.

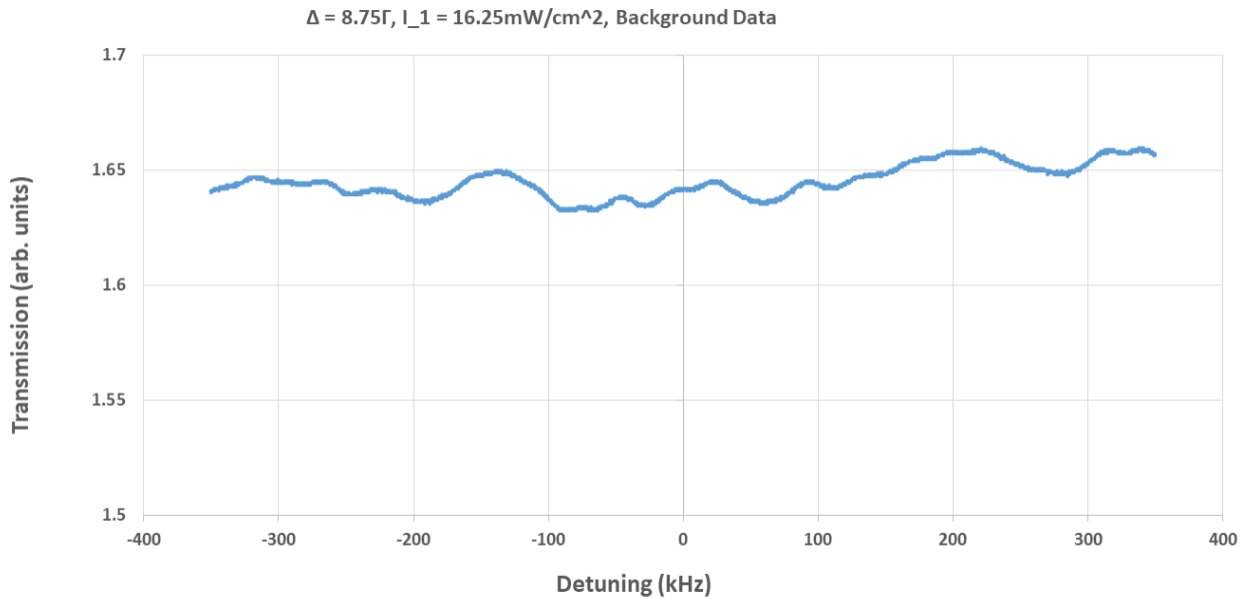


Figure 4.5: Pump-probe spectrum taken in an inverted umbrella lattice at a detuning of 8.75 gamma and 16.25mW/cm^2 axial intensity, 5.84mW/cm^2 beam two and three intensity, and 5.42mW/cm^2 beam four intensity, with the atomic cloud turned off by keeping the magnetic gradient off to capture background signal.

A sample spectrum can be seen in Figure 4.6. In this figure, two peaks, labelled *a* and *b*, can be clearly identified, leading us to believe that a lattice has indeed been formed. Assuming this to be the case, peak *a* is representative of the *z*-vibrational peak. Peak *b*, however, was not expected to be seen for a 1D probe signal, as discussed in section 2.2.1. However, referring back to Figure 3.3, it can be seen that the probe beam also has a small *x* component owing to the slight angle θ_p .

We believe that this second peak forms as a result of this slight misalignment, and represents the x -vibrational peak.

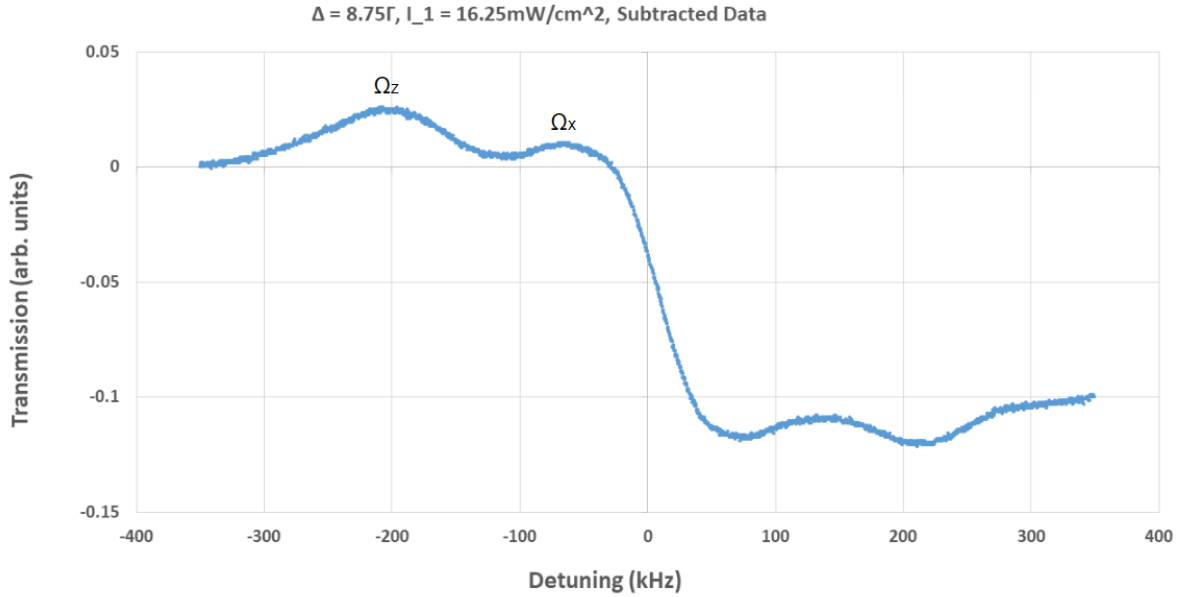


Figure 4.6: Pump-probe spectrum created by subtracting the background data from the raw data point by point. Peak Ω_z corresponds to the z -vibrational frequency, and peak Ω_x to the x -vibrational frequency.

Finally, to confirm that our spectrum is indeed caused by the formation of the lattice, we take a final spectrum with a single lattice beam blocked. By doing so, we keep as much of the experiment the same while ensuring that a lattice is definitely not forming. The results of this run can be seen in Figure 4.7. Comparing this spectrum to the one in Figure 4.6 and the background signal in Figure 4.5, we can be certain that a lattice is indeed forming.

With the lattice spectra resolving very clearly, we can measure the location of the x and z vibrational peaks to determine their respective vibrational frequencies in the lattice. As was the case in the tetrahedral lattice [1], we expect there to be a linear relation between the peak location and the square root of the well depth. In order to quantify this for the inverted umbrella lattice, we plot the peak location as a function of the square root of intensity over detuning, since well depth is known to be proportional to this ratio. We took this for a series of different intensity and detunings, and the results can be seen in Figure 4.8.

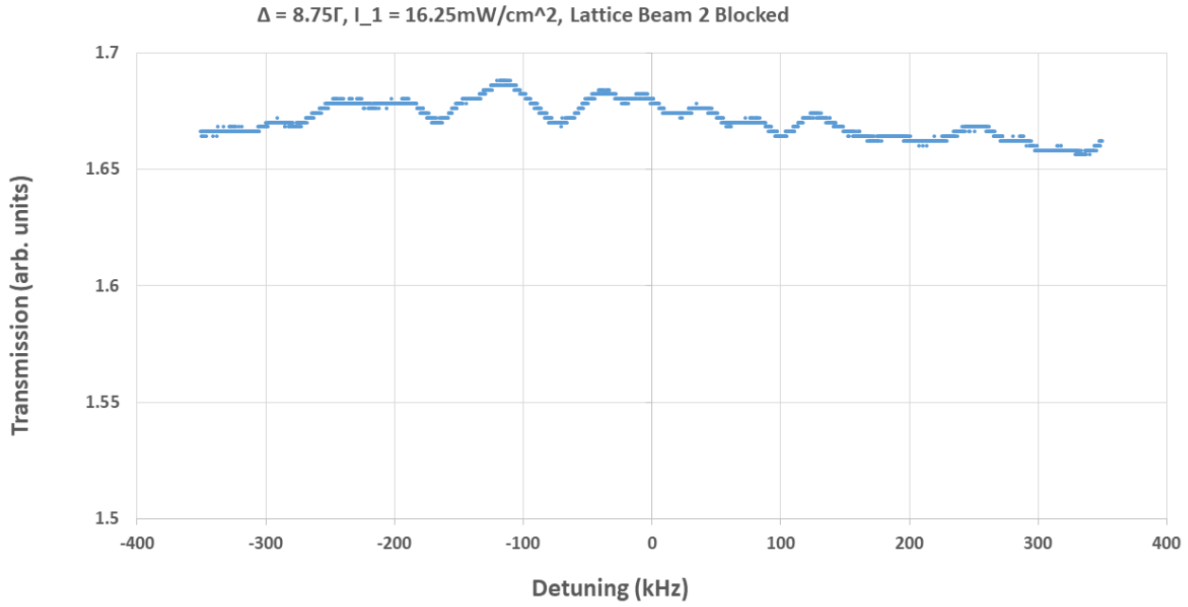


Figure 4.7: Pump-probe spectrum taken in an inverted umbrella lattice at a detuning of 8.75Γ and 16.25mW/cm^2 axial intensity, 5.84mW/cm^2 beam two and three intensity, and 5.42mW/cm^2 beam four intensity, with a single lattice beam blocked.

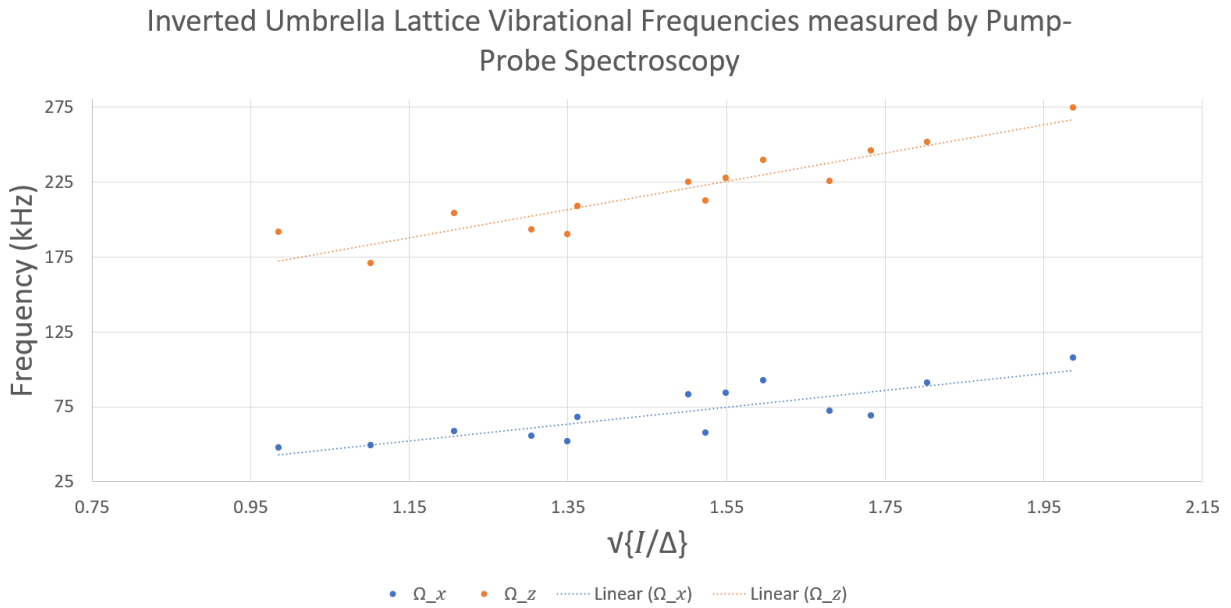


Figure 4.8: Graph of peak locations against $\sqrt{I/\Delta}$. The detuning is expressed as a dimensionless quantity scaled by the natural linewidth Γ , so the x -axis is given in units of $\sqrt{\text{mW/cm}^2}$.

4.2.2 Diffusion Constant and Temperature in 3D Lattice

Once the formation of the lattice has been established, we move on to taking diffusion and temperature measurements in the lattice similarly to how they were performed in the MOT. Due to the lattice being less susceptible to optical phase fluctuations than the molasses, we expect to observe both a lower diffusion constant as well as a lower temperature in the optical lattice than in molasses. Figure 4.9 is a sample data set for diffusion data.

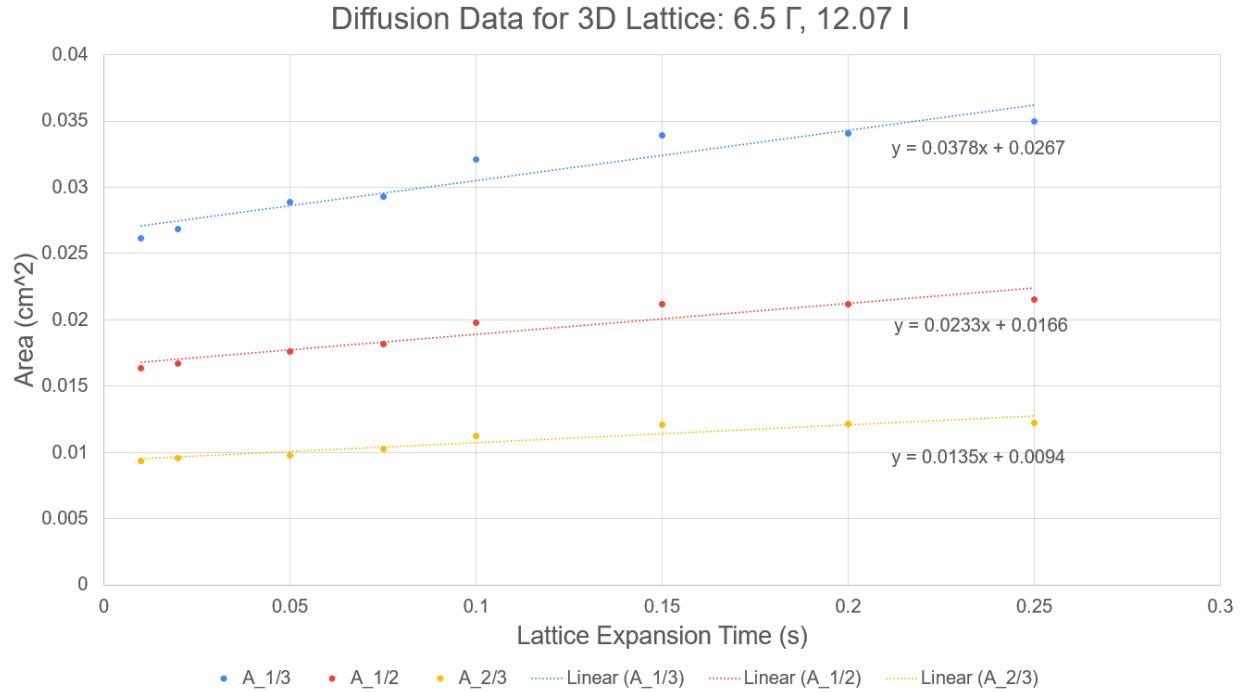


Figure 4.9: Plot of cloud area against lattice expansion time. Data was taken in a 3D inverted umbrella lattice at a detuning of 8.75 γ and 12.07 mW/cm² axial intensity, 4.34 mW/cm² beam two and three intensity, and 4.02 mW/cm² beam four intensity.

Like in the molasses data, we use the area technique from [7] to measure the expansion of the cloud. In the lattice however, the lifetime of the cloud is significantly increased, allowing for longer time intervals to be used. The slope of these lines is used along with equation 3.1 to determine a diffusion constant for the lattice. We found that the $\beta = 2/3$ data is often less reliable, since it is a smaller signal, and thus experiences a correspondingly higher signal to noise ratio since the cloud shape is not perfectly consistent. Comparatively, the $\beta = 1/3$ data frequently has a more robust fit,

as well as a slope that is more consistent with the expected values for diffusion. Data was taken at several different detunings and intensities, and the data is collected in Table 4.3.

Table 4.3: Measured diffusion constants in inverted umbrella lattice

I/Δ	Detuning (Γ)	Intensity (mW/cm^2)	β	Avg. Diffusion Const. (cm^2/s)
1.86	8.75	16.25	1/3	1.6×10^{-3}
1.86	8.75	16.25	1/2	1.0×10^{-3}
1.86	8.75	16.25	2/3	0.3×10^{-3}
1.46	8.75	12.75	1/3	1.4×10^{-3}
1.46	8.75	12.75	1/2	1.2×10^{-3}
1.46	8.75	12.75	2/3	0.7×10^{-3}
1.86	6.5	12.07	1/3	2.6×10^{-3}
1.86	6.5	12.07	1/2	2.5×10^{-3}
1.86	6.5	12.07	2/3	2.5×10^{-3}

We see consistently lower diffusion constants in the lattice than were measured in molasses. Note that the well depth, which is proportional to I/Δ , is repeated in the first and final entries in the table. As with the molasses data, each data set was run twice, and an average is taken to mitigate the fluctuations in the system.

The temperature data in the lattice was collected the same as in molasses, as ballistic expansion time is identical in both systems. Figure 4.10 shows a sample data set from the temperature measurements in the lattice. At the earlier lattice detunings and intensities, temperature data was taken for a variety of lattice expansion times. It is necessary to ensure that the atoms have reached a thermal equilibrium in the lattice, and that Sisyphus cooling has been allowed to take full effect. Furthermore, a balance must be found between a shorter expansion time, which gives a stronger, brighter signal, and a longer expansion time, which causes the cloud to become larger. Previous work done by this group suggests a lattice thermalization time of ~ 3.5 ms [5], so this is considered the minimum lattice expansion time, but at that level the cloud was not large enough for the resolution available to accurately capture the cloud expansion. With all of these criteria in mind, we took temperature data at 10, 20, 50, and 100ms of lattice expansion time for the first lattice parameters, and the data collected is displayed in Table 4.4. Of these lattice expansion times, 50ms was determined to be the most robust, so further data was taken with this lattice expansion time.

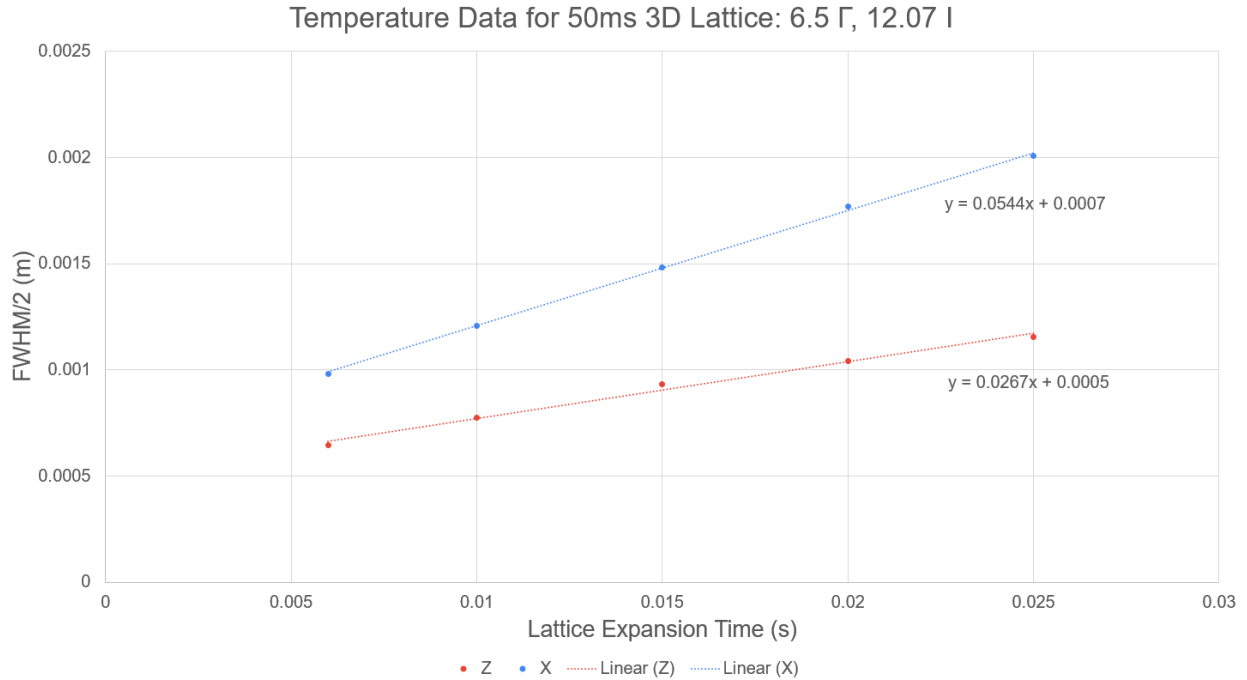


Figure 4.10: Plot of half the full width half maximum against lattice expansion time. Data was taken in a 3D inverted umbrella lattice at a detuning of 8.75 gamma and 16.25mW/cm² axial intensity, 5.84mW/cm² beam two and three intensity, and 5.42mW/cm² beam four intensity.

Table 4.5 shows the data taken at 50ms lattice expansion for a series of different lattice intensities and detunings. The average temperatures were determined using Equation 4.1, the necessity of which is discussed in the surrounding text. These temperatures were in agreement with our expectations, demonstrating a lower temperature in the lattice than in the molasses. Additionally, the lattice data showed a slight difference in the temperature taken along each axis, which comes about as a result of the asymmetric lattice geometry.

Table 4.4: Measured temperatures in inverted umbrella lattice at 8.75Γ detuning and $12.75\text{mW}/\text{cm}^2$ intensity

Lattice Time (<i>ms</i>)	Average Temperature (μK)
10	24.2
20	30.0
50	26.7
100	31.3

Table 4.5: Measured temperatures in inverted umbrella lattice at 50ms lattice time

I/Δ	Detuning (Γ)	Intensity (mW/cm^2)	Avg. Temp (μK)
1.86	8.75	16.25	39.0
1.46	8.75	12.75	25.2
1.86	6.5	12.07	26.9

Chapter 5

Conclusion

5.1 Summary

In this thesis, we demonstrated the functionality of a new form of data collection through measurement of externally verifiable experimental results. By collecting pump-probe spectra, we confirmed the formation of a new lattice using an alternate geometry more conducive to ratcheting experiments. Through fluorescence imaging, we collected data on the diffusion of atoms in both molasses and an optical lattice. Using the same imaging system, we also demonstrated the ability to measure atomic current on the time scale of milliseconds. We successfully observed the impact of Sisyphus cooling and optical confinement on the temperature and diffusion constants of atoms in the optical lattice. The ability to measure both diffusion and atomic current in two dimensions has prepared the lab for the future work into two dimensional ratcheting, rocking ratchets, and absolute negative mobility.

5.2 Future Work

5.2.1 3D Ratchet in Inverted Umbrella Lattice

As discussed in Chapter 2, the Inverted Umbrella Lattice was created with a ratcheting system in mind. By driving the axial beam with a frequency modulated AOM, it is possible to create an

asymmetry in the system that produces an atomic current within the lattice. This is discussed in more detail in [8], and it is planned for this experiment to be pursued in the near future. The implementation of the imaging system makes it much more direct to collect data on atomic current, and steps have been taken to implement the frequency driving.

The main alteration that needs to be made is altering the driving frequency provided to the axial beam AOM from a sinusoidal function to a modulated one, and the AOMs are already connected to Rigol brand waveform generators that accept arbitrary waveforms from an external USB input as .txt files. With the assistance of Miami University's Instrumentation lab, we created a program to combine waveforms with user defined frequency, amplitude, and phase, and save the resulting function as a .txt file. When loaded onto the waveform generator, we have observed that this produces the desired modulated waveform, and work is currently being done to ensure AOM efficiency is maintained while being fed the altered signal.

5.2.2 2D Directionally Arbitrary Ratchet

Another task made possible by the imaging system is observation of two dimensional motion. The work proposed in [3] suggests a system to create 2D ratcheting with full control over the direction of travel. Working in collaboration with the author of [3], we hope to be able to implement such a system in our lab.

For this experiment, new lattice geometry will need to be implemented, since 2D motion is more commonly studied in a 2D lattice to simplify the symmetries across the plane of motion. The proposed lattice geometry is shown in Figure 5.1. The lattice beams 2 and 3 will be driven with modulated frequencies using a similar modulated waveform to those created for the 3D ratchet. If careful attention is paid to the ratios between the parameters of the combined waveforms, the direction of travel can be controlled and predicted, but there is often unexpected results for motion not along a single axis due to coupling between the driving forces [9]. [3] shows theoretical simulations of ways this could be improved, and we hope to experimentally implement some of these methods.

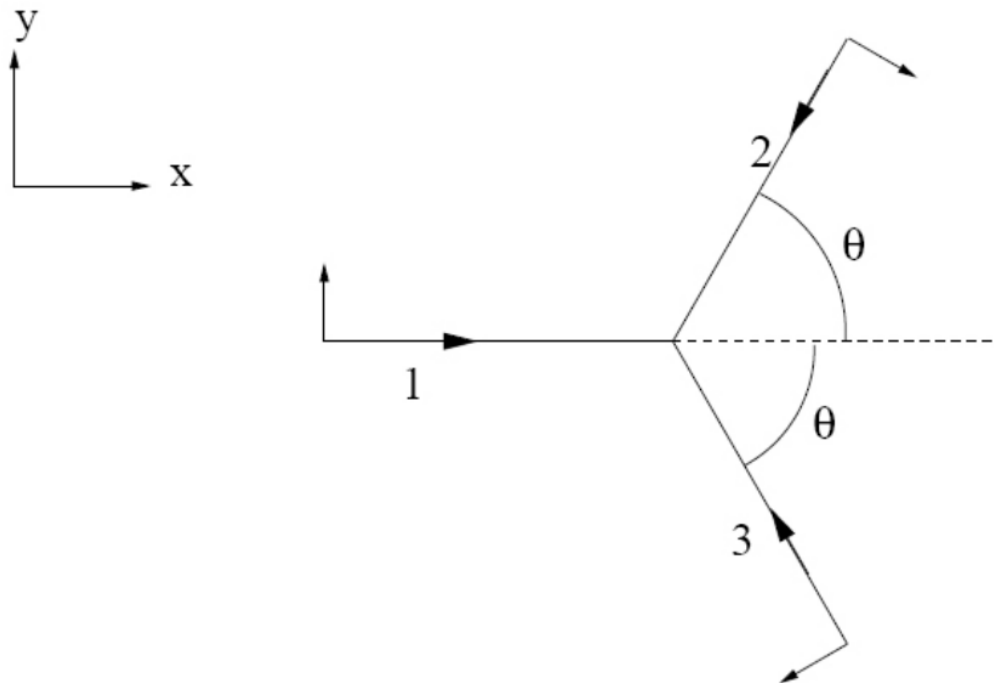


Figure 5.1: Geometry of the proposed 2D lattice. In the ideal case, $\theta = 120^\circ$, but the configuration of the vacuum chamber windows in our lab may result in a value of $\theta = 115^\circ$. Image taken from [9].

Appendix A

Suppressing Mode Hops in Commercial Laser Systems

Mode hops are a somewhat unavoidable issue that can make it impossible to find a clean spectrum to frequency lock to. Over time, the amount of sweep between mode hops gradually shrinks, and it may become necessary to take steps to reverse the process so that an entire spectrum can fit in a mode hop free region. While the home built lasers have a relatively simple process to correct these issues, the many interconnected electrical components and processes on the commercial system make it somewhat more complicated to approach this without making unintended changes to the rest of the system. There is a general guide to this process in Appendix C of the External Cavity Diode Laser Controller (DLC) manual, but we are able to skip the majority of the steps presented there as we are starting with a system that is already very close to full functionality. Below, the steps taken on our specific laser system are laid out and, if followed closely, should drastically improve the amount of mode hop free scanning range.

1. Begin by fully decreasing the span knob. Gradually increase the span value until you encounter a mode hop, then navigate away from it using the frequency knob on the DLC. Continue until there are mode hops on both sides of the oscilloscope screen.
2. Make small adjustments to the current and frequency knobs to increase the distance between adjacent mode hops as far as possible. It may be necessary to continue to increase the span

knob if this process significantly improves the spacing between the hops. If you are able to get a full spectrum with just this step, it may be unnecessary to continue. If, however, the current and frequency knobs are insufficient, BIAS optimisation will be required.

3. Ensure the BIAS dipswitch is on. The switches can be found under the top cover of the DLC, and a description of each can be found in chapter 2 of the manual. Figure A.1 shows the location of the switches under the cover. The BIAS dipswitch is switch 4. (Note: Ensure all components of the diode laser are off, not simply in standby, before removing the cover.)
4. Adjust the BIAS trimpot found on the front panel of the DLC to further spread out adjacent mode hops. The first time this step is performed, it may not be a drastic increase, but adjust to the maximum possible distance.
5. Repeat steps 2 and 4 in an iterative manner, until no mode hops are observed at your current span level.
6. Begin to increase the span level. It will likely be the case that mode hops are again encountered as the span level is increased, in which case make small adjustments to the BIAS, current, and frequency knobs until the mode hops once again are out of the screen, then resume increasing the span level.
7. Slowly and carefully following step 6 should allow for a full spectrum to be obtained at maximum span level. Lock the laser, and ensure the MOT can still be obtained.



Figure A.1: Image of the inside of the DLC. The dipswitches are in the bottom left, a bright red panel. The BIAS dipswitch is the fourth from the right.

Appendix B

MATLAB Analysis Codes

Throughout the course of this thesis, the data collected was routinely analyzed through the use of a number of MATLAB codes. This appendix will discuss the purpose of each code, explain how to use the code on future data, and present the code itself. The code is also backed up to the lab's google drive, and the versions found there are also commented to allow for a more detailed understanding of the code and to aid in any edits that may be required. The comments were omitted here for space considerations.

The first code that is commonly used is Textifier. This code's purpose is to quickly and easily convert files to text files. The reason this code was created is that the current LabVIEW program saves the image files without an extension, and the following MATLAB codes use the .txt extension name to identify text files. Rather than edit all other codes, we found it to be quicker and easier to convert the files to .txt extensions using this code. In order to use this code, the files to be converted will need to be saved to a single folder with no other contents. When the code is run, the user will be called to select a folder, which should be that folder. The code will then create exact copies of all files within that folder, but with a text file extension. The original files will be saved and placed into a new sub-folder called 'Original Data' within the main folder. The code will also display a warning message upon completion, stating that it was unable to delete the 'Original Data' folder, but this is as intended and can safely be ignored.

```
1 function Textifier = Textifier()
```

```

2 oldDir = cd;
3 startdir = uigetdir('', 'Where is the file(s) saved?');
4 cd(startdir);
5 files = dir(fullfile(startdir, '*.*'));
6 files = files(~[files.isdir]);
7 mkdir(startdir, 'OriginalData');
8 for k = 1:length(files)
9     file = fullfile(startdir, files(k).name);
10    [tempDir, tempFile] = fileparts(file);
11    OGDDir = append(tempDir, '\OriginalData');
12    copyfile(file, fullfile(tempDir, [tempFile, '.txt']));
13    copyfile(file, fullfile(OGDDir, tempFile));
14 end
15 delete *.*;
16 cd(oldDir);

```

The following code is the primary analysis code used for extracting useful data from the image files. It is called FWHMfinder, which is short for Full Width Half Maximum Finder, which is the primary purpose of the code. In short, given an image, this code will return the FWHM of the image. It also has sections that can be commented in or out of the code that also find the relative center of mass of the cloud. These two measurements are the essential components of the diffusion, temperature, and ratcheting measurements performed in this thesis. In order to do this, the code uses the built in MATLAB fitting program to fit a 2D Gaussian curve to the image, which can be thought of as two 1D Gaussians set perpendicular to each other, where the intensity of each pixel represents its z value. The parameters used in the Gaussian fit include both the standard deviation and the center of the curve. Additionally, if multiple files have been collected at a certain timing sequence, as we commonly do to reduce error induced by random fluctuations, this code will automatically take those images and create a composite image from the average pixel intensities. The code also can be fed a file of background images to be subtracted from the primary image files.

In order to use the code, the image files to be analyzed must be placed together in a single folder. It is not necessary for them to be the only things present in the folder, but they must be the only files with .txt extensions. A separate folder with the background files must also be present, and the background text files must have the same dimensions as the image files. The user will be prompted twice. The first time, the user should select the folder containing the image files, and the second time, the user should select the folder containing the background files. The code will then take all text files in the image folder, average them, take all the text files in the background folder, average them, and then subtract the averaged background from the averaged image. This background corrected image will then be scaled such that the maximum value is one, and a 3D mesh grid plot will be generated of the resulting file, where the z-axis is the intensity of each pixel. The code then fits two Gaussian functions to the array, one in x and one in y, and uses the values of the origin and the standard deviation of the function to calculate and display the center and FWHM of the image, both with units of centimeters.

There is a known issue with this code, that at higher timing sequences (typically around 100 milliseconds of molasses or 30 ms of ballistic expansion time), MATLAB's native fitting function has trouble determining an accurate FWHM of the image. If the user notices the Gaussian is approaching the edges of the mesh grid when it is plotted, it is advisable to check the FWHM by hand as well, using the mesh grid. At low to mid timing sequences, however, the computer generated values were found to match quite well with the hand calculated ones.

```
1 function FWHMfinder = FWHMfinder()
2 tic
3 olddir = cd;
4 BinLevel = 4;
5 folder = uigetdir('', 'Select the Image Folder');
6 disp(folder)
7 cd(folder);
8 filelist = dir('*.txt');
9 j2 = 1;
```

```

10 threshold = 0;
11 for j = 1:length(filelist)
12     tempcell{j2} = load(filelist(j).name);
13     intensitysum = sum(sum(tempcell{j2}));
14     [intensitymax, index] = max(tempcell{j2}(:));
15     [intensitymin, index] = min(tempcell{j2}(:));
16     if intensitymax < threshold
17         tempcell{j2} = [];
18         disp(['(max) tossed file number ', num2str(j), ' from
                folder ', folder]);
19     elseif intensitymin < 0
20         tempcell{j2} = [];
21         disp(['(min) tossed file number ', num2str(j), ' from
                folder ', folder]);
22     else
23         j2 = j2 + 1;
24     end
25 end
26 image = cat(3,tempcell{1:end});
27 Avgimg = mean(image,3);
28 backfolder = uigetdir('','Select the Background Folder');
29 disp(backfolder)
30 cd(backfolder);
31 backfilelist = dir('*.txt');
32 for j = 1:length(backfilelist)
33     backtempcell{j} = load(backfilelist(j).name);
34 end
35 backimage = cat(3,backtempcell{1:end});

```

```

36 Avgback = mean(backimage,3);
37 Avgimg = Avgimg - Avgback;
38 Corimg = Avgimg./max(max(Avgimg));
39 PrettyPic{1} = Corimg;
40 figure
41 mesh(PrettyPic{1});
42 [xsize,ysize] = size(Corimg);
43 if xsize == ysize
44     [xo,yo,zo] = prepareSurfaceData(1:xsize,1:ysize,Corimg);
45 elseif xsize > ysize
46     Corimg = Corimg(1:ysize,1:ysize);
47     [xo,yo,zo] = prepareSurfaceData(1:ysize,1:ysize,Corimg);
48 else
49     Corimg = Corimg(1:xsize,1:xsize);
50     [xo,yo,zo] = prepareSurfaceData(1:xsize,1:xsize,Corimg);
51 end
52 ft = fit([xo,yo],zo,'exp(-(((x-xcen)^2)/vx + ((y-ycen)^2)/vy))','
          StartPoint',[10000,5000,xsize/2,ysize/2],'Robust','Bisquare');
53 vx = ft.vx./2;
54 vy = ft.vy./2;
55 xcen = ft.xcen;
56 ycen = ft.ycen;
57 FWHMX = 2.355*sqrt(vx);
58 FWHMY = 2.335*sqrt(vy);
59 % disp(['FWHM in x = ', num2str(FWHMX)]);
60 % disp(['FWHM in y = ', num2str(FWHMY)]);
61 % disp(['Relative x-center is x_0 = ', num2str(xcen)]);
62 % disp(['Relative y-center is y_0 = ', num2str(ycen)]);

```

```

63 FWHMXcm = FWHMX*(4.31e-4)*BinLevel;
64 FWHMYcm = FWHMY*(4.31e-4)*BinLevel;
65 xcencm = xcen*(4.31e-4)*BinLevel;
66 ycencm = ycen*(4.31e-4)*BinLevel;
67 disp(['FWHM in x (in cm) = ', num2str(FWHMXcm)]);
68 disp(['FWHM in y (in cm) = ', num2str(FWHMYcm)]);
69 %disp(['Relative x-center is x_0 (in cm) = ', num2str(xcencm)]);
70 %disp(['Relative y-center is y_0 (in cm) = ', num2str(ycencm)]);
71 cd(olddir);
72 clear
73 toc

```

AFinder, seen below, is an extension of FWHMFinder, but calculates the expansion of the cloud in a different way. Instead of determining the FWHM, it instead totals the number of pixels above a certain ratio of the maximum power as a measurement of area, akin to what is done in [7]. It is used in the exact same way as FWHMFinder, and outputs three values for three different ratio levels.

```

1 function AFinder = AFinder()
2 tic
3 olddir = cd;
4 BinLevel = 4;
5 folder = uigetdir('', 'Select the Image Folder');
6 disp(folder);
7 cd(folder);
8 filelist = dir('*.txt');
9 image = cat(3, tempcell{1:end});
10 Avgimg = mean(image, 3);
11 cd(olddir);
12 backfolder = uigetdir('', 'Select the Background Folder');

```

```

13 disp(backfolder);
14 cd(backfolder);
15 backfilelist = dir('*.txt');
16 for j = 1:length(backfilelist)
17     backtempcell{j} = load(backfilelist(j).name);
18 end
19 backimage = cat(3,backtempcell{1:end});
20 Avgback = mean(backimage,3);
21 Avgimg = Avgimg - Avgback;
22 Corimg = Avgimg./max(max(Avgimg));
23 PrettyPic{1} = Corimg;
24 figure
25 mesh(PrettyPic{1});
26 [xsize,ysize] = size(Corimg);
27 if xsize == ysize
28     [xo,yo,zo] = prepareSurfaceData(1:xsize,1:ysize,Corimg);
29 elseif xsize > ysize
30     Corimg = Corimg(1:ysize,1:ysize);
31     [xo,yo,zo] = prepareSurfaceData(1:ysize,1:ysize,Corimg);
32 else
33     Corimg = Corimg(1:xsize,1:xsize);
34     [xo,yo,zo] = prepareSurfaceData(1:xsize,1:xsize,Corimg);
35 end
36 [xsize, ysize] = size(Corimg);
37 Area13 = 0;
38 Area12 = 0;
39 Area23 = 0;
40 for k = 1:xsize

```

```

41     for p = 1:ysize
42         if Corimg(k,p) >= 0.333
43             Area13 = Area13 + 1;
44         end
45         if Corimg(k,p) >= 0.5
46             Area12 = Area12 + 1;
47         end
48         if Corimg(k,p) >= 0.667
49             Area23 = Area23 + 1;
50         end
51     end
52 end
53 Area13 = Area13*(4.31e-4)*(4.31e-4)*BinLevel*BinLevel;
54 Area12 = Area12*(4.31e-4)*(4.31e-4)*BinLevel*BinLevel;
55 Area23 = Area23*(4.31e-4)*(4.31e-4)*BinLevel*BinLevel;
56 disp(['A 1/3 (in cm^2) = ', num2str(Area13)]);
57 disp(['A 1/2 (in cm^2) = ', num2str(Area12)]);
58 disp(['A 2/3 (in cm^2) = ', num2str(Area23)]);
59 cd(olddir);
60 toc

```

The final analysis code used is SDGFFinder, or Standard Deviation Gaussian Fit Finder. This code operates very similarly to FWHMFinder, in that it uses MATLAB's fitting function to determine the FWHM and center of an input image. This code, however, does not use the averaging features of FWHMFinder to produce a single FWHM, but rather applies the fitting to each file individually, and takes the standard deviation of the set of FWHM values for the current timing sequence. In order to use the code, the image files for which the standard deviation is to be found must be placed together in a single folder, saved with .txt file extensions. It is often the case that this is the same folder that was used for the primary image folder in FWHMFinder. The user will

be called a single time, and the folder containing these files should be selected. The code will then fit a Gaussian curve to each image individually, produce a FWHM for each, and then take the standard deviation of this data set. Since the fitting function is typically applied roughly ten times, this function can take a while to run. Additionally, in its current state the code does not support background subtraction.

```
1 function SDGFFinder = SDGFFinder()
2 tic
3 oldDir = cd;
4 binLevel = 4;
5 threshold = 0;
6 folder = uigetdir('Select the Data Folder');
7 cd(folder);
8 fileList = dir('*.txt');
9 FWHMXData = [];
10 FWHMYData = [];
11 for j=1:length(fileList)
12     disp(['Crunching file ', num2str(j), '...']);
13     data = load(fileList(j).name);
14     [intensityMax, ~] = max(data(:));
15     [intensityMin, ~] = min(data(:));
16     if intensityMax < threshold
17         disp(['File', num2str(j), 'has intensity below threshold
18             tolerance and has been discarded.']);
19         continue
20     elseif intensityMin < 0
21         disp(['File', num2str(j), 'has intensity less than zero
22             and has been discarded.']);
23         continue
24     end
25 end
```

```

22     else
23         scaledData = data./max(max(data));
24         [xSize, ySize] = size(scaledData);
25         if xSize == ySize
26             [xo,yo,zo] = prepareSurfaceData(1:xSize,1:ySize,
                scaledData);
27         elseif xSize > ySize
28             scaledData = scaledData(1:ySize,1:ySize);
29             [xo,yo,zo] = prepareSurfaceData(1:ySize,1:ySize,
                scaledData);
30         else
31             scaledData = scaledData(1:xSize,1:xSize);
32             [xo,yo,zo] = prepareSurfaceData(1:xSize,1:xSize,
                scaledData);
33     end
34     ft = fit([xo,yo],zo,'exp(-(((x-xcen)^2)/vx + ((y-ycen)^2)
                /vy))','StartPoint',[10000,5000,xSize/2,ySize/2],'
                Robust','Bisquare');
35     vx = ft.vx./2;
36     vy = ft.vy./2;
37     %xcen = ft.xcen;
38     %ycen = ft.ycen;
39     FWHMX = 2.355*sqrt(vx);
40     FWHMY = 2.335*sqrt(vy);
41     FWHMXcm = FWHMX*(4.31e-4)*binLevel;
42     FWHMYcm = FWHMY*(4.31e-4)*binLevel;
43     %xcencm = xcen*(4.31e-4)*BinLevel;
44     %ycencm = ycen*(4.31e-4)*BinLevel;

```

```

45         FWHMXData = cat(1, FWHMXData, FWHMXcm);
46         FWHMYData = cat(1, FWHMYData, FWHMYcm);
47     end
48 end
49 %disp(FWHMXData);
50 %disp(FWHMYData);
51 Sx = std(FWHMXData);
52 Sy = std(FWHMYData);
53 Ax = mean(FWHMXData);
54 Ay = mean(FWHMYData);
55 disp(folder);
56 disp(['The standard deviation of the FWHM along x is: ', num2str(
        Sx)]);
57 disp(['The standard deviation of the FWHM along y is: ', num2str(
        Sy)]);
58 %disp(['The average FWHM along x is: ', num2str(Ax)]);
59 %disp(['The average FWHM along y is: ', num2str(Ay)]);
60 cd(oldDir);
61 toc

```

Bibliography

- [1] A. Staron, K. Jiang, C. Scoggins, D. Wingert, D. Cubero, and S. Bali, “Observation of stochastic resonance in directed propagation of cold atoms,” *Phys. Rev. Res.*, vol. 4, p. 043211, Dec 2022.
- [2] D. Cubero, “Brillouin propagation modes of cold atoms in dissipative optical lattices,” 2022. Accepted for publication in *Phys. Rev. E*. arXiv:2208.08206.
- [3] D. Cubero and F. Renzoni, “Control of transport in two-dimensional systems via dynamical decoupling of degrees of freedom with quasiperiodic driving fields,” *Phys. Rev. E*, vol. 86, p. 056201, Nov 2012.
- [4] V. Lebedev and F. Renzoni, “Two-dimensional rocking ratchet for cold atoms,” *Phys. Rev. A*, vol. 80, p. 023422, Aug 2009.
- [5] A. Staron, “Stochastic resonances and velocity sorting in a dissipative optical lattice.” Master’s Thesis, Miami University, 2020.
- [6] E. Clements, “Characterization of optical lattices using pump-probe spectroscopy and fluorescence imaging.” Master’s Thesis, Miami University, 2016.
- [7] T. Hodapp, C. Gerz, C. Furtlehner, C. I. Westbrook, W. D. Phillips, and J. Dalibard, “Three-dimensional spatial diffusion in optical molasses,” *Applied Physics B*, vol. 60, pp. 135–143, Feb 1995.
- [8] R. Gommers, “Symmetry and transport in cold atom ratchets.” PhD Thesis, University College London, 2007.

- [9] V. Lebedev, “Ac driven ratchets for cold atoms: Beyond 1d rocking ratchets.” PhD Thesis, University College London, 2009.
- [10] S. Bhar, M. Swar, U. Satpathi, S. Sinha, R. Sorkin, S. Chaudhuri, and S. Roy, “Measurements and analysis of response function of cold atoms in optical molasses,” *Opt. Continuum*, vol. 1, pp. 171–188, Feb 2022.
- [11] G. Grynberg and C. Robilliard, “Cold atoms in dissipative optical lattices,” *Physics Reports*, vol. 355, no. 5, pp. 335–451, 2001.
- [12] C. Scoggins, “Brillouin propagation of cold atoms - velocity-matching or mechanical resonance?.” Master’s Thesis, Miami University, 2022.
- [13] F.-R. Carminati, L. Sanchez-Palencia, M. Schiavoni, F. Renzoni, and G. Grynberg, “Rayleigh scattering and atomic dynamics in dissipative optical lattices,” *Phys. Rev. Lett.*, vol. 90, p. 043901, Jan 2003.
- [14] L. Sanchez-Palencia, F.-R. Carminati, M. Schiavoni, F. Renzoni, and G. Grynberg, “Brillouin propagation modes in optical lattices: Interpretation in terms of nonconventional stochastic resonance,” *Phys. Rev. Lett.*, vol. 88, p. 133903, Mar 2002.
- [15] A. J. Hachtel, M. C. Gillette, E. R. Clements, S. Zhong, M. R. Weeks, and S. Bali, “Note: Design and implementation of a home-built imaging system with low jitter for cold atom experiments,” *Review of Scientific Instruments*, vol. 87, p. 056108, 05 2016.
- [16] K. Pandey, “Determining the damping coefficient of cold atoms in a magneto optical trap.” Master’s Thesis, Miami University, 2023.